

Observations of wind farm wake recovery at an operating wind farm

Raghavendra Krishnamurthy¹, Rob K. Newsom¹, Colleen M. Kaul¹, Stefano Letizia², Mikhail Pekour¹, Nicholas Hamilton², Duli Chand¹, Donna Flynn¹, Nicola Bodini², Patrick Moriarty²

¹Pacific Northwest National Laboratory, Richland, 99352, United States of America

5 ²National Renewable Energy Laboratory, Golden, 80401, United States of America

Correspondence to: Raghavendra Krishnamurthy (raghu@pnnl.gov)

Abstract. The interplay of momentum ~~within~~ surrounding wind farms significantly influences wake recovery, affecting the speed at which wakes return to their free-stream velocities. Under stable atmospheric conditions, wind farm wakes can extend over considerable distances, leading to sustained vertical momentum flux downstream, with variations observed throughout the diurnal cycle. Particularly in regions such as the US Great Plains, stable conditions can induce low-level jets (LLJs), impacting wind farm performance and power output. This study examines the implications of wake recovery using long-term observations of vertical momentum flux profiles across diverse atmospheric conditions. In these observations, several key findings were observed, such as a) low-level jet heights are altered downstream of a wind farm, especially when the LLJs are below 250 m above ground level, b) a notable impact of low-level jet height on wake recovery is observed using momentum flux profiles at upwind and downwind location, wherein LLJs between 250 m and 500 m above ground level resulted in larger momentum transfer within the wake (i.e., smaller velocity deficit) compared to LLJs below 250 m above ground level, c) largest momentum flux variability is observed during stable atmospheric conditions, with non-negligible variability observed during neutral and unstable atmospheric conditions, ed) detection of wake effects is almost always observed throughout the atmospheric boundary layer height, and finally ed) enhancement of wake recovery is observed in the presence of propagating gravity waves. These insights deepen our understanding of the intricate dynamics governing wake recovery in wind farms, advancing efforts to model and predict their behaviour across varying atmospheric contexts. In addition, the performance of large-eddy simulation-based semi-empirical internal boundary layer height model estimates incorporating real-world atmospheric and turbine inputs was evaluated using observations during low-level jet conditions.

25 1 Introduction

Wind turbine wakes, i.e., velocity deficits due to extraction of kinetic energy from an operating wind turbine, are observed to extend several kilometres during stable atmospheric conditions both onshore and offshore (Hirth et al., 2012; Banta et al., 2015; Krishnamurthy et al., 2017; Fernando et al., 2019; Ahsbabs et al., 2020; Zhan et al., 2020). Wind farm wakes from a large cluster of wind turbines in mesoscale model simulations can reach over 50 km downwind under stable atmospheric conditions (Platis et al., 2018; Lundquist et al., 2019, Schneemann et al., 2020). Large-eddy simulations of large

wind farms also show that wind farm wakes can alter the surface momentum and heat fluxes (Calaf et al., 2011). Wind farm wakes are known to impact local meteorological conditions by, for instance, increasing or decreasing the temperature and enhancing turbulence downwind of a wind farm (Baidya Roy et al., 2004; Smith et al., 2013; Siedersleben et al., 2018; Miller and Keith, 2018, Bodini et al., 2021), although the intensity of impact depends on atmospheric stability, local atmospheric processes, orientation of the wind farms, downwind distance, number and operative regimes of wind turbines, etc.

In operational wind farms, intra-farm wakes can result in significant power losses and it is important to understand the dissipation of wakes within a wind farm. The effect of a wind turbine is to decrease the mean velocity and increase the turbulent kinetic energy above the rotor layer (the layer from the bottom of the wind turbine blade tip to the top of the blade tip, VerHulst and Meneveau, 2014). The turbulent transport term in a steady-state filtered-energy equation includes the entrainment of mean momentum due to turbulence $\overline{u_i u_j u_k}$ and the entrainment of turbulent kinetic energy due to fluctuating velocities $0.5 \overline{u_i u_j u_k}$ (Allaerts and Meyers, 2017). Downwind of a wind farm the recovery of a wind turbine wake within a rotor layer largely occurs due to enhanced entrainment of vertical momentum flux from the boundary layer (Abkar and Porte-Agel, 2013; Yang et al., 2014; VerHulst and Meneveau, 2014; Abkar and Porte-Agel, 2014; Lu and Porte-Agel, 2015). The maximum energy produced by a large (>100MW) land-based wind farm is then constrained by the momentum flux between the surrounding atmosphere and the flow within the wind farm. Therefore, measuring the entrainment of mean momentum due to turbulence upwind and downwind of an operational wind farm can provide insight into the momentum balance of wakes within a wind farm. The momentum balance can be a function of various locally observed atmospheric phenomena, such as low-level jets (LLJ), gravity waves, high shear/veer events etc. Atmospheric stability is known to impact the extent of wake propagation downstream (Hansen et al., 2012, Barthelmie et al., 2012, Hirth et al., 2012, Smith et al. 2013, Krishnamurthy et al., 2017, Lundquist et al., 2019). In conjunction with some of the local atmospheric features, the transfer of momentum within and outside the surrounding wind farm can show drastic spatial and temporal heterogeneity.

Today's Wind-wind turbines operate within the lowest 300 m of the atmospheric boundary layer (ABL), and in offshore or stable atmospheric conditions the ABL is lower than 300 m (Shaw et al., 2022). Although wind farms operate within 300 m above ground level, their impacts can be observed through the entire depth of the boundary layer. Therefore, to accurately assess such impacts, observations of mean and turbulent characteristics of wind and temperature should be extended up to the top of the ABL. Remote sensing instruments, such as Doppler lidars, are capable of estimating the mean winds over-within the ABL (Frehlich, 1994, Frehlich, 2001, Peña et al., 2009, Krishnamurthy et al., 2013, Newsom and Krishnamurthy, 2021) as well as turbulence with accuracy comparable to sonic anemometers, which are considered a standard for atmospheric turbulence measurements (Frehlich and Cornman, 2001, Frehlich et al., 2006, Banakh and Smalikho, 1997, Krishnamurthy et al., 2012, Sathé et al., 2015, Bonin et al., 2017, Wildmann et al., 2019). Certain observational studies have validated the propagation of wakes for long distances downwind (more than 20 rotor diameters

65 [RDs]), using targeted long-range scanning radar measurements (Hirth et al., 2012; Ahsbabs et al., 2020), satellite-based radar observations (Djath et al., 2018) and airborne observations (Lampert et al., 2020). But other observations have also shown that wake deficits are small at larger RDs (~26 RDs) downstream of a multimegawatt wind farm (Smith et al., 2013). As wake extents grows laterally downwind of a wind farm, measuring velocity deficits at larger downwind distances can get very challenging, due to small deficits. Therefore, assessing the impact of wakes purely based on wind speed and turbulence intensity estimates at targeted observational locations, would not provide a good representation of wake dissipation. Large-
70 eddy simulations have previously shown momentum deficit estimates within and above the wind farm rotor layer at large downwind distances (Stevens ~~et al.~~, 2016, Gadde and Stevens, 2021) and provide more realistic information about the influence of wind farm wakes on the atmospheric boundary layer. Therefore, accurately measuring momentum deficits at various downwind distances of a wind farm, rather than just mean winds and turbulence intensity profiles, might provide a
75 better assessment of wind farm wakes. Recent studies have focused on observing momentum flux variability around a wind farm using in-situ observations on an aircraft (Syed et al., 2023), but there has not been a study, as per the authors knowledge, looking at any systematic and statistically significant trends in vertical momentum flux profiles under a variety of atmospheric conditions within-surrounding an operational wind farm. Therefore, it would be essential to know under what atmospheric conditions wakes recover faster, thereby reducing the impact on downwind wind farms or turbines for
80 optimal siting of wind farms/turbines and power production estimates.

Gravity waves and atmospheric bores are ubiquitous in the SGP region (Carbone et al., 1990, Davis et al., 2003, Geerts et al., 2017). Although most frequently observed during nocturnal and stable atmospheric conditions, they vary significantly in their period and amplitude. These nocturnal convective systems typically accompany high winds, intense rain and/or hail and sometimes tornadoes (Maddox, 1980). The forecast skill of such atmospheric events is relatively low in both
85 numerical weather prediction models and coarse-grid climate models (Davis et al., 2003, Pritchard et al., 2011). They also typically include a low-level jet within the atmospheric boundary layer, which supports the moisture transport above the stable boundary layer over SGP (Berg et al., 2015, Krishnamurthy et al., 20221a). Primarily gravity waves create wave-like oscillations in the atmosphere due to the presence of a density gradient and bore disturbances are shown to have a significant upward displacement of wind within the troposphere (Rottman and Simpson, 1989, Parsons et al., 2019). Such wave-like
90 disturbances when reaching the surface, can create undulations in the mean winds depending on the period and wavelength of the wave. Mountain waves have previously been known to impact the power production of a wind farm (Draxl et al., 2021) but the impact of propagating gravity waves on wake recovery is not very well understood.

Wind farms create a step change in surface roughness and when the atmospheric boundary layer height (δ) is larger than the surface momentum roughness (z_{om}), an internal boundary layer (δ_{IBL}) is developed in the region downstream of the surface discontinuity (Elliot 1958, Taylor 1969, Calaf et al., 2013, Stevens et al., 2016, Krishnamurthy et al., 2023). The boundary layer flow is observed to adjust to this new surface condition and grows with downstream distance (x). The growth of the internal boundary layer is a function of mean wind, thermal stratification or atmospheric stability, inversion height of the ABL, and surface turbulence characteristics. In the presence of a wind farm, the growth of an internal boundary layer is
95

also a function of the mean wind turbine spacing and characteristics of the wind turbine performance (Calaf et al., 2013, Stevens 2016, Stevens and Meneveau, 2017). The momentum flux into a wind farm replenishes the wake of a wind farm and the height of the internal boundary layer can reach up to δ . During stable atmospheric conditions, δ_{IBL} will grow to reach δ within a short distance from the leading edge of a wind farm, resulting in a fully developed IBL. While most of the existing studies have been based on high-resolution models, limited long-term observations of δ_{IBL} growth are available in the literature. Syed et al., 2023 showed spatial variability of momentum flux measurements from in-situ sensors onboard an aircraft upstream, above, and downstream of a wind farm, but did not provide a vertical profile up to the boundary layer. Therefore, estimating profiles of momentum flux up to the boundary layer depth can provide insights into the impact of internal boundary layers on wind farm dynamics.

Dimensional arguments show that at far field, large x , as equilibrium conditions prevail, i.e., $u_*^d/u_*^u = \mathcal{F}_1(z_0^u/z_0^d)$, where u_*^d and z_0^d are downwind friction velocity and roughness length, \mathcal{F}_1 is an unknown function, while the superscripts u refers to upwind estimates (Krishnamurthy et al., 2023). In the presence of a wind farm, the model presented in Calaf et al., 2010 assumes two constant stress levels, above ($u_{*,hi}$) and below ($u_{*,lo}$) the wind turbine, with the difference between those momentum layers given as

$$u_{*,hi}^2 = u_{*,lo}^2 + \frac{1}{2} c_{ft} (\langle \bar{u} \rangle_{z_h})^2 \quad (1)$$

where $\langle \bar{u} \rangle_{z_h}$ is the horizontally and time averaged velocity at hub-height, $c_{ft} = \frac{\pi C_T}{(4S_x S_y)}$, C_T is the turbine coefficient of thrust, and lateral and transverse spacing between the wind turbines is given by S_x and S_y . Using a logarithmic wind profile formulation ($U(z) = u_* \ln(z/z_0)/\kappa$), where κ is von Karman constant (0.4), a relationship for wind turbine roughness height of the wind farm ($z_{0,hi}$) can be estimated (Stevens 2016). Thereby, the growth of the internal boundary layer due to a wind farm can be estimated using (Willingham et al., 2014)

$$\frac{\delta_{IBL}(x)}{z_{0,hi}} = \frac{\delta_{IBL}(0)}{z_{0,hi}} + C_1 \left(\frac{x}{z_{0,hi}} \right)^{4/5} \quad (2)$$

where, x is the downwind distance, $\delta_{IBL}(0)$ is the internal boundary layer height of the wind turbine rotor top at the first row of the wind farm (equal to the wind turbine blade upper tip height), $z_{0,hi}$ is the surface roughness due to the presence of a wind farm, and C_1 is a growth constant (0.28) estimated from large-eddy simulation models (Calaf et al., 2010, Stevens, 2016). The wind farm surface roughness is a function of the upwind surface friction velocity, wind turbine and farm parameters, and inflow mean wind conditions within the wind turbine rotor layer. Existing large-eddy simulations estimates of internal boundary layers have typically used idealized conditions while real-world atmospheric conditions estimate of IBL.

130 might differ considerably due to competing atmospheric conditions. Therefore, observations of internal boundary layer
growth are important to understand the impact of wind farms on the ABL and thereby the momentum balance surrounding a
wind farm and associated wake replenishment.

In this paper we investigate the wake recovery of a wind farm, by investigating the momentum balance (primarily
135 mean streamwise momentum flux [$\langle u'w' \rangle$]) surrounding an operational wind farm near the Atmospheric Radiation
Measurement (ARM) program Southern Great Plains (SGP) sites in Oklahoma during various site-specific atmospheric
phenomena. Momentum flux profiles from scanning Doppler lidars and surface sonic anemometers are estimated for both
upwind and downwind locations relative to the wind farm. ~~These novel observations reveal the temporal and spatial~~
~~variability of momentum balance within and above the wind farm wakes during regional specific atmospheric conditions.~~
140 ~~Profiles also show the growth of the internal boundary layer and allow quantification of the accuracy of current large-eddy~~
~~simulation based approximations in estimating the growth of the internal boundary layer (IBL).~~ ~~Theoretical preliminaries~~
~~are provided in Section 2, details about turbulence retrievals from sonic anemometers and Doppler lidars is provided in~~
~~Section 3, and i~~Information about the field campaign and site characteristics are given in Section 4.2. Momentum flux
profiles upwind and downwind of an operational wind farm during site-specific atmospheric conditions are discussed in
145 Section 5.3. Wind farm IBL measurements, comparison of data with theoretical models are given in Section 6.4 and results
are summarized in Section 7.5.

2 Mathematical Preliminaries

150 Wind farms create a step change in surface roughness and when the boundary layer height (δ) is larger than the
surface momentum roughness (z_{0m}), an internal boundary layer (δ_{IBL}) is developed in the region downstream of the surface
discontinuity (Elliot 1958, Calaf et al., 2013, Stevens et al., 2016, Krishnamurthy et al., 2022). The boundary layer flow is
observed to adjust to this new surface condition and grows with downstream distance (x). The growth of the internal
boundary layer is a function of mean wind, thermal stratification or atmospheric stability, inversion height of the ABL, and
155 surface turbulence characteristics. In the presence of a wind farm, the growth of an internal boundary layer is also a function
of the mean wind turbine spacing and characteristics of the wind turbine performance (Calaf et al., 2013, Stevens 2016,
Stevens and Meneveau, 2017). The turbulent entrainment of mean kinetic energy into a wind farm replenishes the wake of a
wind farm and the height of the internal boundary layer can reach up to δ . During stable atmospheric conditions, δ_{IBL} will
grow to reach δ within a short distance from the leading edge of a wind farm, resulting in a fully developed IBL. While
160 most of the existing studies have been based on high resolution models, limited long term observations of δ_{IBL} growth are
available in the literature. Syed et al., 2023 showed spatial variability of momentum flux measurements from in situ sensors

onboard an aircraft upstream, above, and downstream of a wind farm, but did not provide a vertical profile up to the boundary layer. Therefore, estimating profiles of momentum flux up to the boundary layer depth can provide insights into the impact of internal boundary layers on wind farm dynamics.

Dimensional arguments show that at far field, large x , as equilibrium conditions prevail, i.e., $u_x^d/u_x^u = \mathcal{F}_x(z_0^d/z_0^u)$, where u_x^d and z_0^d are downwind friction velocity and roughness length, while the superscripts u , refers to upwind estimates (Krishnamurthy et al., 2022). In the presence of a wind farm, the model presented in Calaf et al., 2010 assumes two constant stress levels, above ($u_{x,ht}^+$) and below ($u_{x,ht}^-$) the wind turbine, with the difference between those momentum layers given as

$$u_{x,ht}^2 = u_{x,te}^2 + \frac{1}{2} c_{JT} (\langle \bar{u} \rangle z_H)^2, \quad (1)$$

where $\langle \bar{u} \rangle z_H$ is the horizontally and time averaged velocity at hub height, $c_{JT} = \frac{\pi C_T}{(4S_x S_y)}$, C_T is the turbine coefficient of thrust, and lateral and transverse spacing between the wind turbines is given by S_x and S_y . Using a logarithmic wind profile formulation ($U(z) = u_* \ln(z/z_0)/k$), where k is von Karman constant (0.4), a relationship for wind turbine roughness height of the wind farm ($z_{0,ht}$) can be estimated (Stevens 2016). Thereby, the growth of the internal boundary layer due to a wind farm can be estimated using (Willingham et al., 2014)

$$\frac{\delta_{IBL}(x)}{z_{0,ht}} = \frac{\delta_{IBL}(0)}{z_{0,ht}} + C_i \left(\frac{x}{z_{0,ht}} \right)^{4/5}, \quad (2)$$

where, x is the downwind distance, $\delta_{IBL}(0)$ is the internal boundary layer height of the wind turbine rotor top at the first row of the wind farm, $z_{0,ht}$ is the surface roughness due to the presence of a wind farm, and C_i is a growth constant (0.28) estimated from large eddy simulation models (Calaf et al., 2010, Stevens, 2016). The wind farm surface roughness is a function of the upwind surface friction velocity, wind turbine and farm parameters, and inflow mean wind conditions within the wind turbine rotor layer. Existing large eddy simulations estimates of internal boundary layers have typically used idealized conditions while real world atmospheric conditions estimate of IBL might differ considerably due to competing atmospheric conditions. Therefore, observations of internal boundary layer growth are important to understand the impact of wind farms on the ABL and thereby the momentum balance within a wind farm and associated wake replenishment.

3 Flux estimation algorithms and approach

190 Herein we provide details of the algorithms used to estimate momentum fluxes from surface based anemometers and scanning Doppler lidars, and a methodology to estimate the height of the internal boundary layer from upwind and downwind momentum flux profiles.

3.1 Momentum flux estimates from sonic anemometers

195 Sonic anemometers are considered a standard for estimating atmospheric turbulence parameters (Wilezak et al., 2001, Wilezak et al., 2019, Fernando et al., 2019). Three dimensional (3-D) acoustic anemometers provide measurements of winds and temperature at high temporal frequency (> 20 Hz), which supports calculation of higher order statistics with good accuracy (Cook and Sullivan, 2020). The sign conventions of the 3-D winds vary for different manufacturers and for Gill Sonic anemometers, which were deployed for this project, the sign conventions are defined as positive for upward vertical wind component (w) and upward atmospheric fluxes, u wind component (North-South) is positive towards North and v wind component (East-West) is positive towards the West. The raw and flux data files are generated as per Cook and Sullivan, 2020, and contain 30 minutes of post-processed data and estimates of turbulent fluxes. The sonic data is post-processed by first applying a de-spiking procedure (Goring and Nikora, 2002) to remove any data anomalies and a 2-axis coordinate rotation is performed (Wilezak et al., 2001), which ensures $\langle w \rangle = \langle v \rangle = 0$ and $\langle u_x \rangle = U$, where U is the mean wind speed, u_x is the stream-wise component and $\langle \cdot \rangle$ is a 30-minute temporal average. To estimate the fluxes, the average of each variable is estimated over a 30-minute (non-overlapping) window and no detrending of the data is performed to estimate the velocity fluctuations. The stress tensor is then computed using 30-minute measurements of velocity fluctuations and assumed to be statistically stationary over the averaging window.

200

205

3.2 Momentum flux profiles from Doppler lidars

210 A brief description of the method to estimate momentum flux profiles from lidars is given below (Eberhard et al., 1989; Mann et al., 2010). The radial velocity (v_r) equation of a Doppler lidar is given by:

$$v_r(R, \theta) = u \sin \varphi \cos \theta + v \sin \varphi \sin \theta + w \cos \varphi, \quad (3)$$

215 where, R is the range, φ is the half opening angle of the conical cone (30°), θ is the azimuthal direction of the lidar beam (0 degrees is North), and $[u, v, w]$ are the wind components at each range gate center. The variance of v_r is given by:

$$220 \quad \sigma^2[v_r(R, \theta)] = \sigma_u^2 \sin^2 \varphi \cos^2 \theta + \sigma_v^2 \sin^2 \varphi \sin^2 \theta + \sigma_w^2 \cos^2 \varphi + 2(u'v') \sin^2 \varphi \cos \theta \sin \theta + 2(u'w') \cos \varphi \sin \varphi \cos \theta + 2(v'w') \cos \varphi \sin \varphi \sin \theta, \quad (4)$$

where $\langle \rangle$ represents 30 minute averaging and $[u', v', w']$ are the velocity fluctuations. One can estimate the streamwise momentum flux components $\langle (u'w') \rangle$ by calculating the radial velocity variance in the upwind and downwind directions over 30 minutes (Eberhard et al., 1989; Mann et al., 2010), which is then given by:

$$225 \quad \langle (u'w') \rangle = \frac{\sigma^2[v_{r-down}] - \sigma^2[v_{r-up}]}{2 \sin 2\varphi}, \quad (5)$$

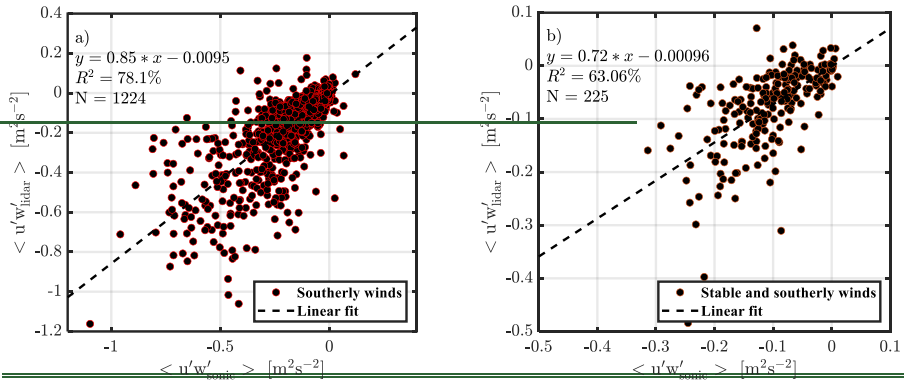
where, $\sigma^2[v_{r-down}]$ and $\sigma^2[v_{r-up}]$ are the radial velocity variances from the nearest downwind and upwind azimuth angles relative to the mean wind direction, respectively and φ is the mean wind direction. The nearest up and down

230 radial velocities from the azimuth angles are picked for each 30 minute sample and given range gate wind direction estimate. It can be noted from Eq. 5 that in a positively sheared turbulent flow, $\sigma^2[v_{up}] > \sigma^2[v_{down}]$, i.e., the upwind variances are typically larger than downwind variances. The effect of measurement volume is not considered in this analysis and has been shown to have a minimal impact on the streamwise momentum flux measurements for Doppler lidars (Mann et al., 2010).

235 For evaluating the accuracy of the algorithm, continuous Velocity Azimuth Display (VAD) scans at the same elevation and azimuth angles are required to calculate the variance of the radial velocity along each beam. From October 8, 2020, to January 14, 2021, continuous eight point Planned Position Indicator (PPI) scans (Az = 45° and el = 60°) were conducted at the Atmospheric Radiation Measurement (ARM) Southern Great Plains (SGP) Central Facility to support an ongoing field campaign. The mean wind direction (ϕ) at each height is calculated using the approach of Newsom et al. (2017), wherein a chi square distribution is fit to estimate the horizontal wind vector. Each beam was averaged for 6 seconds to provide a robust estimate of radial velocity and study the effect of noise from individual radial velocity measurements (Frehlich et al., 2001). This averaging could underestimate the variance observed by the lidar. During this study, each 360 degree wind profile was completed in 1 minute. This provided the ability to calculate variance of radial velocity along each beam and the momentum flux profile using Eq. 5.

240

245 Momentum flux estimates from sonic anemometer data on a 60 m tower were calculated using the eddy correlation method (Stull, 1988). Along wind momentum flux ($u'v'$) estimates from the sonic anemometer at 60 m and lidar at 75 m from southerly wind directions are shown in the Figure 1a.



250 **Figure 1:** 20 minute averaged along wind momentum flux ($\langle u'w' \rangle$) measurements from lidar at 75 m and sonic at 60 m AGL from October 8, 2020, to January 14, 2021 at ARM SGP central facility, for a) southerly wind directions under all atmospheric conditions and b) southerly wind directions under very stable atmospheric conditions ($10 \text{ m} < L < 150 \text{ m}$). A linear fit between the measurements ($y = m * x + c$), coefficient of determination (R^2), and number of samples (N) are also shown.

255

Doppler lidar ($\langle u'w' \rangle$) measurements are observed to correlate reasonably well to sonic anemometer ($\langle u'w' \rangle$) measurements, with slope of 0.85 and a coefficient of determination of 78%. To quantify the effect of stable atmospheric conditions on the accuracy of lidar derived momentum flux estimates, the stability of the atmosphere was determined using the Obukhov length, L , given by

260
$$L = \frac{u_*^2 T}{kg \langle w'^2 \theta'_v \rangle} \quad (6)$$

where T is the air temperature, g is the acceleration due to gravity, and $\langle w'^2 \theta'_v \rangle$ is the kinematic heat flux. During stable atmospheric conditions, given the amount of stratification within the lidar probe volume, the lidar could be measuring very different atmospheric conditions compared to a sonic anemometer. Figure 1b shows measurements from southerly wind directions and very stable atmospheric conditions ($10 \text{ m} < L < 150 \text{ m}$). The coefficient of determination is observed to reduce

265 during stable conditions to 62%, although the wind speeds are observed to correlate well under all conditions. The transfer
of momentum is lowest in stable atmospheric conditions and therefore smaller momentum flux estimates are observed. From
a purely statistical standpoint, the smaller magnitude of the fluxes also contributes to reducing the coefficient of
determination, since under these conditions the contribution of instrumental and statistical noise to the physical variability of
270 relatively larger. The scatter between lidar and sonic measurements are primarily due to (a) 15 m vertical and 250 m
horizontal separations between sonic anemometer and lidar measurements, (b) low temporal sampling of the lidar
measurements, and (c) spatial averaging of the lidar pulse (range gate 30 m). These effects amplify during stable
atmospheric conditions and result in larger scatter between measurements. Previous observations of momentum flux from
profiling Doppler lidars have shown a similar accuracy when compared to sonic anemometers at various heights above
ground level (Mann et al., 2010). Overall, the performance of the algorithm is expected to be adequate for the analysis being
275 conducted in this article.

2 Field campaign and site characteristics

Oklahoma ranks third in the United States for installed wind capacity, providing over 37,418 Giga Watt hour (GWh) of
280 electricity in 2022. The state generated approximately 44% of its electricity from wind energy in 2022, the third highest in
the country, and provided enough electricity to power the millions of U.S. homes. The landscape and topographic flows
around SGP are relatively simple compared to complex terrain sites with low wind speed interannual variability (< 3%) and
therefore are favored by wind farm developers (Krishnamurthy et al., 2021 a). To investigate the interaction between wind
farms and the ABL and improve our understanding of wind turbine and wind plant-farm wake effects, the U.S. Department
285 of Energy (DOE) funded a field campaign, American WAKE experieMeNt (AWAKEN), within and adjacent to King Plains
wind farm near Enid, Oklahoma (Debnath et al., 2023, Moriarty et al., 2023). Figure 1~~Figure 2~~ shows the domain of the
AWAKEN field experiment, various locations with instruments deployed, and operational wind turbines within the domain.
Several remote sensing and in-situ sensors were deployed, please see Moriarty et al., 2024 for additional details of the site
setup and layout. In this article, data from primarily two instrumented sites are used for data analysis. Site A2 is the inflow
290 site and site H the outflow site to King Plains wind farm during southerly wind directions. Figure 1~~Figure 2~~ shows a picture
of both the sites and various instruments deployed. Site A2 was instrumented with a Scanning Doppler lidar, short-range
vertical profiling lidar, surface sonic anemometer, and a surface meteorological station, while site H had a scanning Doppler
lidar, microwave radiometer, and two disdrometers. Both the scanning lidars were oriented close to North, like the sonic
anemometers. Azimuth and elevation offsets for the scanning lidars were identified by using the stationary tower near the
295 wind farm as a hard target. These offsets were used to correcting the observed azimuth and elevation angles from the
scanning Lidars (as described in Newsom and Krishnamurthy, 2020). Frequent hard target scans were conducted to evaluate
any drift in the levelling of the lidar, and none was observed during the period of study. The internal pitch and roll of the
lidars were constantly below 0.1 degrees. In addition, boundary layer height estimates from a ceilometer at site A1 (also an

inflow site) were used to evaluate the impact of boundary layer structure on wind farm wake propagation. The wind turbines
300 deployed at the King Plains wind farm are GE 2.8 MW machines with a hub-height of 89 m and a rotor diameter (RD) of
127 m. The average lateral and transverse distance in southerly wind directions between wind turbines (over the Eastern
sector of the King Plains wind farm, intersecting sites A1 and H) is approximately 3.15 RD (S_x) and 14.57 RD (S_y). Site A2
is approximately 40 RD upwind of the first row of the King Plains wind farm, site A1 is approximately 2 RD upwind, and
site H is approximately 22 RD downwind of the last row of the King Plains wind farm. [Additional details on various
305 instruments deployed at the AWAKEN site can be found in Moriarty et al., 2024.](#)

Both scanning lidars installed at A2 and H run a composite scan routine that includes 20 minutes of six-beam
profiling (Sathe et al., 2015) and 10 minutes of vertical stares. Wind profiles from 100 to 3000 m are obtained by applying
the well-established least squares fit to the radial velocity measurement six-beam [\(Newsom and Krishnamurthy, 2020\)](#).
310 Momentum flux is also estimated through the technique described in [Seet. 3.2 Appendix A.2](#) applied to the upstream and
downstream beams based on the selected wind direction sector of interest [\(see Eq. A.3\)](#). In the following, momentum flux
measurements from the surface sonic anemometer at the respective site are also combined with the lidar retrieval to extend
the observable range down to the surface. [Measurements only from southerly wind directions, specifically from 166 degrees
to 190 degrees are considered in this analysis. Additionally, since removing all outliers from lidar observations is
315 challenging, the median of the sample will be presented in the remainder of the manuscript.](#)

[Figure 2 Figure 3a](#) shows the wind rose at 105 m above ground level from Doppler lidar measurements collected
from March 17, 2023, to September 10, 2023. Wind directions are predominantly southerly during the duration of the study.
[Figure 2 Figure 3b](#) shows the distribution of various atmospheric stability conditions as a function of wind direction.
320 Atmospheric conditions were divided into various classes based on the Obukhov length (L) scale as provided in
Krishnamurthy et al., 2021 [a and Table 1 below](#). [Obukhov length, \$L\$, is given by](#)

$$L = - \frac{u_*^3 T}{kg \langle w' \theta'_v \rangle} \quad (3)$$

[where \$T\$ is the air temperature, \$g\$ is the acceleration due to gravity, and \$\langle w' \theta'_v \rangle\$ is the kinematic heat flux from sonic
325 anemometers.](#)

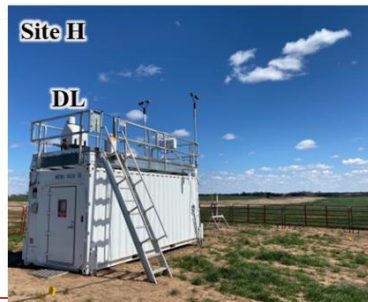
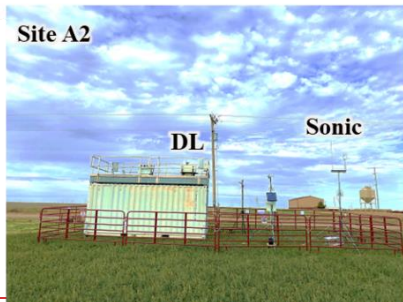
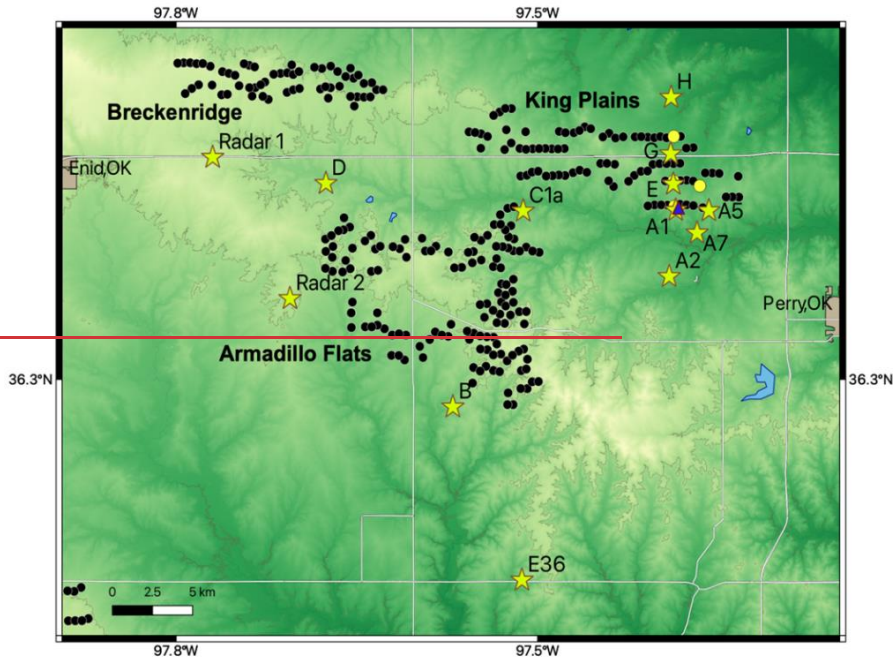
At SGP C1 (which is ~21 km north of King Plains wind farm), stable atmospheric conditions are observed for more
than 50% of the time. During neutral conditions, a larger percentage of winds are either easterly or northerly. It is important
to note that surface atmospheric stability might not always be representative of conditions at elevated levels, especially
during transition periods (i.e., during sunset and sunrise).

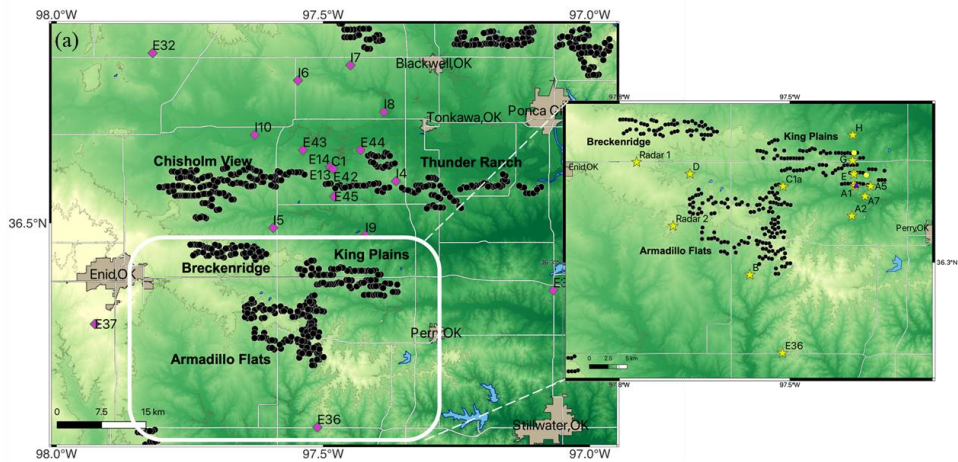
Formatted: Font: 10 pt, Not Bold

Formatted: Font: 10 pt, Not Bold

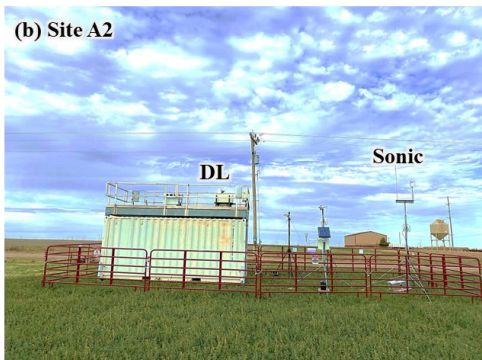
Table 1. Stability classification based on L thresholds.

<u>Stratification</u>	<u>L</u>
<u>Very stable</u>	<u>$10 < L < 50$</u>
<u>Stable</u>	<u>$50 < L < 200$</u>
<u>Near-neutral stable</u>	<u>$200 < L < 500$</u>
<u>Neutral</u>	<u>$L > 500$</u>
<u>Near-neutral unstable</u>	<u>$-500 < L < -200$</u>
<u>Unstable</u>	<u>$-200 < L < -100$</u>
<u>Very unstable</u>	<u>$-100 < L < -50$</u>





(b) Site A2



(c) Site H

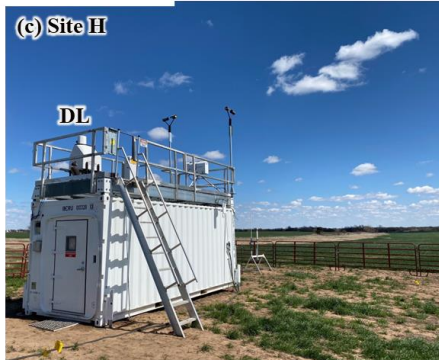


Figure 12. (top) Southern great plains area with location of the AWAKEN field campaign (white box) shown, various sites deployed (yellow stars and circles) during the AWAKEN field campaign, DOE ARM sites (magenta diamonds), and the wind turbines (black circles) in the area (Moriarty et al., 2024). (b) Images of instruments deployed at site A2 (inflow to King Plains wind farm for dominant southerly wind directions) and (c) site H (downwind of King Plains wind farm) are also shown at the bottom.

335

340

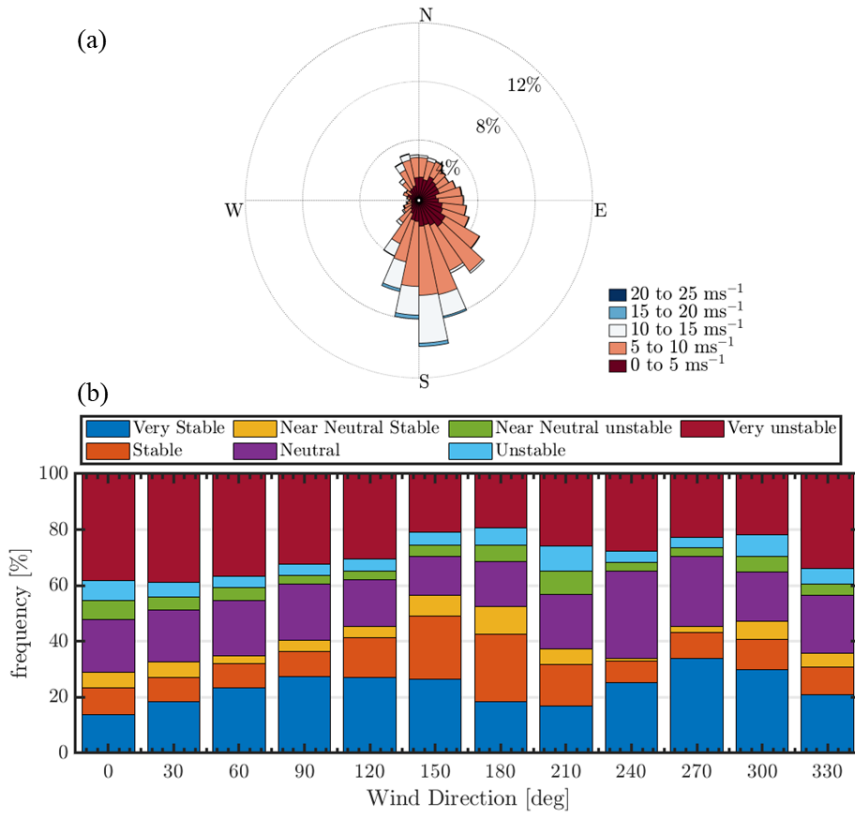


Figure 23. (top) Wind rose at 105 m AGL from a Doppler lidar at SGP central facility during all atmospheric conditions. (bottom) Atmospheric stability classification as a function of wind direction from March 17, 2023, to September 10, 2023.

345 Various atmospheric stability classes are distinguished based on L and defined in Krishnamurthy et al. (2021) and Table 1.

4.1 Internal boundary layer estimates from observations

350 As discussed earlier, an internal boundary layer is developed due to a step change in surface roughness. Turbulence is expected to be higher within the internal boundary layer (downwind of the surface roughness) compared to inflow (upwind of the surface roughness). Wind farms create a step change in surface roughness and are known to develop internal boundary layers downwind of a wind farm (Calaf et al., 2013, Stevens and Meneveau, 2017). In addition to the roughness

impacts of the wind turbines, the wind farm developed internal boundary layer is convolved with the wake of the wind turbines, which create additional momentum deficits downwind of the wind farm. Internal boundary layers can be estimated from a velocity profile, by identifying a kink in the velocity profile (Garratt et al., 1990). Although this method provides a general trend, it is known to be not very accurate. An alternative technique, proposed in Stevens 2016, is being implemented here, where the difference in streamwise momentum flux profiles upwind and downwind of a surface roughness change are used to estimate the growth of the internal boundary layer. Figure 4 shows the median streamwise momentum flux and wind speed both upwind and downwind of a wind farm from southerly wind directions ($166^\circ < \phi < 190^\circ$) from over 6 months of data collected near an operational wind farm (more details in Section 3). Vertical momentum flux is responsible for the influx of momentum into the wake of a wind farm. Larger streamwise momentum flux deficits above the wind farm are mainly observed due to turbulence and shear generated by the wind turbines. Wind turbine wakes enhance vertical mixing above a wind farm, which results in a downward flow of momentum. The internal boundary layer height (δ_{IBL}) is the height when the upwind and downwind momentum flux estimates are within 1% of each other above the wind farm. In Figure 4, the δ_{IBL} is approximately equal to 780 m above ground level (AGL). Therefore, the median impact of the wind farm is observed up to 780 m AGL during southerly wind directions under all atmospheric conditions. Similar technique can be used to estimate internal boundary layer height from models or formulations as shown in Eq 2 above. As previously mentioned δ_{IBL} can sometimes be inaccurately estimated using the difference between upwind and downwind wind speed profiles, where δ_{IBL} is shown to be ~600 m AGL in Figure 4.

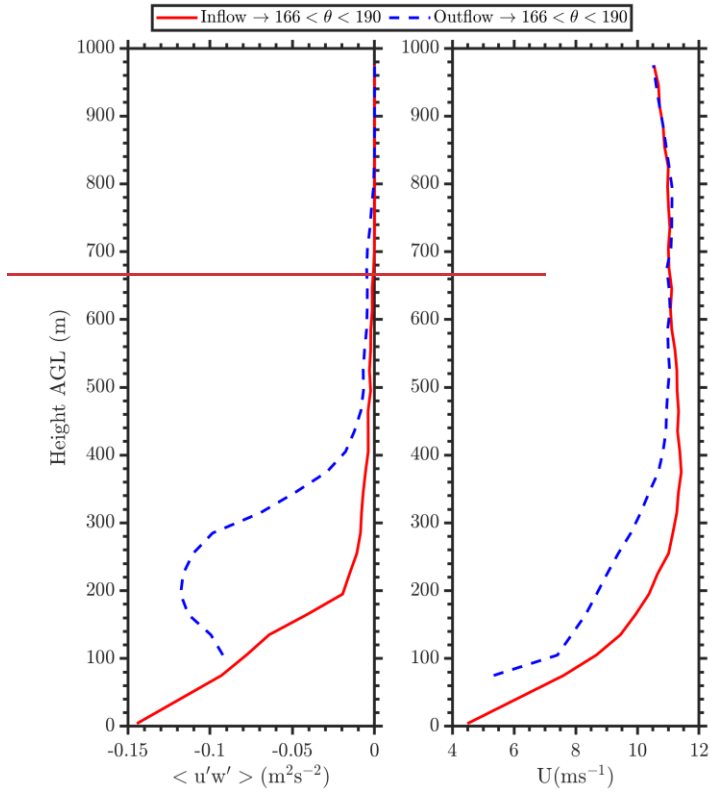


Figure 4. (left) Median streamwise momentum flux and (right) wind speed profiles site A2 or the upwind site (red) and site H or the downwind site (blue dashed) of the King Plains wind farm in Oklahoma. Only measurements from southerly wind directions (ϕ) between 166 degrees and 190 degrees are shown.

3 Wake Recovery Observations

To minimize the impacts of wakes from neighboring wind farms (including the Breckinridge and Armadillo Flats wind farms shown in Figure 1 Figure 2) in our analysis and to measure the impact of wakes from at least 3 rows of wind turbines, measurements only from southerly wind directions, especially from 166 degrees to 190 degrees are considered. Since the wind directions are predominantly southerly, sufficient data is available to accurately estimate the mean trends of

momentum flux during specific atmospheric conditions. Below, statistics of momentum flux variability under different atmospheric conditions, such as varying levels of thermal stratification (stability), ~~low-level jets~~LLJs, high wind shear and veer conditions, ABL depth, and atmospheric gravity waves are assessed.

385

5.3.1 Impact of atmospheric stability on wake recovery

As shown in ~~Figure 2~~Figure 4b, when winds are southerly the atmospheric stability is predominantly (>50%) stable near the surface, with neutral conditions occurring about 20% of the time and unstable conditions observed for the remainder. ~~Figure 3~~Figure 5 shows median momentum flux ($\langle u'w' \rangle$) profiles from the downwind (site H) and upwind (site A2) locations during stable, neutral, and unstable atmospheric conditions. In general, we observe higher negative momentum flux upwind of the wind farm near the surface with an asymptotic behaviour eventually reaching zero near δ , like a canonical atmospheric boundary layer. Downwind of the wind farm, enhanced $-(u'w')$ is observed due to the shear and turbulence generated by the wind turbines. Stable conditions are observed to show larger deviations in momentum flux downwind of the wind farm compared to neutral or unstable atmospheric conditions. The sign of momentum flux is tied to the vertical wind shear, as for sustenance of turbulence within a wind farm an increase in wind shear (positive) should result in negative momentum flux downwind of a wind farm.

390

395

Therefore, in stable atmospheric conditions, due to large (positive) wind shear, the momentum flux must be negative to create downwind turbulence. ~~As mentioned earlier, the wind plant-farm wake propagates longer in stable conditions due to lower ambient turbulence compared to convective conditions, therefore at site A2 which is approximately 22 RD downwind of the last row of the King Plains wind farm, the region of enhanced vertical momentum flux due to the wind farm is expected to be more persistent and varies with the diurnal cycle (Figure 3~~Figure 5a). ~~In Figure 3~~Figure 5b and ~~Figure 3~~5c, larger momentum flux estimates are observed near the surface during unstable and neutral atmospheric conditions compared to stable conditions. ~~For neutral conditions, since the shear is less positive and higher ambient turbulence compared to stable conditions is expected, the downwind wind turbine generated momentum flux is expected to be lower or not persistent, and wakes are not expected to propagate longer distances. Under neutral conditions, where shear is less positive and ambient turbulence is higher compared to stable conditions, the momentum flux generated by downwind wind turbines is anticipated to be lower or less persistent. Consequently, wakes are not expected to travel as far. But in Figure 3~~Figure 5b, significant momentum flux deficits are still observed at 22 RDs downwind during neutral conditions. A couple of possible reasons for this could be due to a) misclassification of atmospheric stability from surface flux measurements, i.e., surface atmospheric stability at hub-height is not representative of the true atmospheric state and b) higher wind shear observed during neutral conditions resulting in more negative momentum fluxes within the wind farm wake. Larger the vertical momentum flux faster the wake velocity recovers to a freestream value (Syed et al., 2023). While during unstable atmospheric conditions, wakes are expected to dissipate faster (convective mixing of the atmospheric boundary layer) and due to low wind shear, the momentum flux deficits are expected to be significantly lower. In ~~Figure~~

400

405

410

Formatted: Font: 10 pt, Not Bold

Formatted: Font: 10 pt, Not Bold

Formatted: Font: 10 pt, Not Bold

Formatted: Font: 10 pt, Not Bold

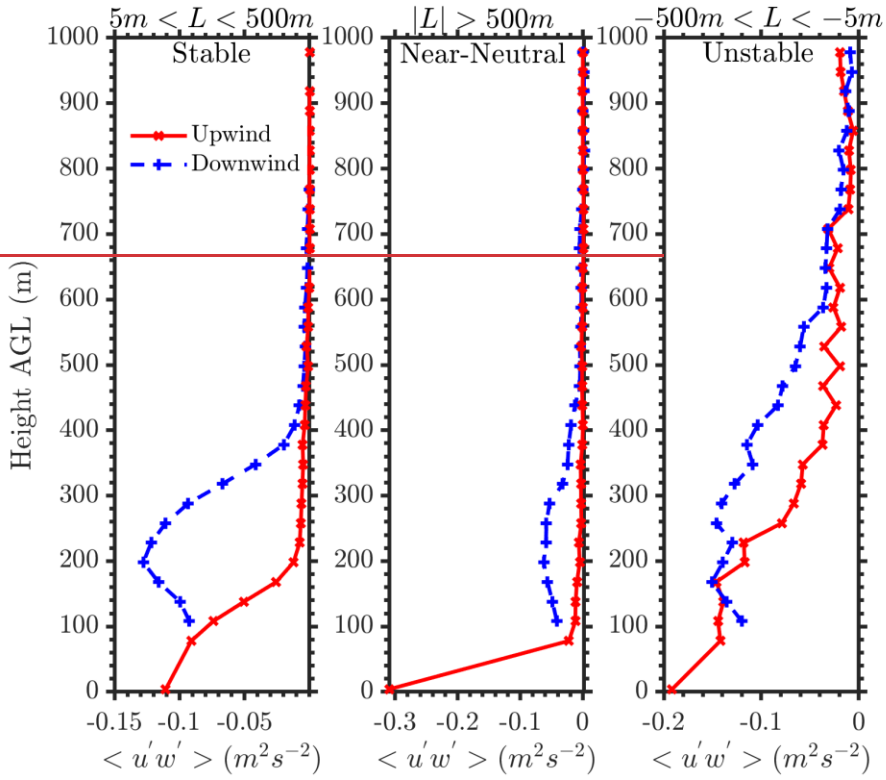
Formatted: Font: 10 pt, Not Bold, Do not check spelling or grammar

Formatted: Font: 10 pt, Not Bold

Formatted: Font: 10 pt, Not Bold

415 [3Figure 5c](#), it is evident that during unstable conditions the momentum flux deficits are lower but still observed 22 RD
downwind. One potential reason for deficits observed during unstable conditions at 22 RDs downwind could be the impact
of ~~conventional~~ [convective](#) updrafts or downdrafts on propagation of wake downwind of a wind farm (Berg et al., 2017,
Wang et al., 2020). Additional analysis is required, ideally using high-resolution large-eddy simulations, to truly evaluate
the impact of updrafts and downdrafts on wind farm wakes. Overall, the median deficit observed over King Plains wind
420 farm shows that the flow disturbance downwind of a wind farm can extend long distances (at least 22 RDs) in every
atmospheric condition. Such differences are generally not very evident from solely observing wind profile observations
upwind and downwind of a wind farm.

As mentioned earlier, no observations of vertical profiles of momentum flux have been recorded to date within an
operational wind farm, therefore, there is limited knowledge on the height at which the peak transfer of momentum occurs
425 downwind of a wind farm. It is well known that the peak velocity deficit (upwind – downwind velocity) generally occurs at
hub-height, but there are no observations showing the peak momentum deficit above the wind farm. Based on large-eddy
simulation results, the peak momentum deficit is expected to occur near the upper edge of the wind turbine rotor layer
(Abkar and Porte-Agel, 2015), but based on observations at King Plains wind farm, in stable conditions, at 22 RD
downwind, peak momentum flux is consistently observed at ~0.36 RD above the wind farm. Therefore, the mean kinetic
430 energy entrainment height into the wake is observed to occur higher than traditional LES models. Additional comparisons
between LES models and observations are required to further evaluate the wake recovery processes within a wind farm
wake.



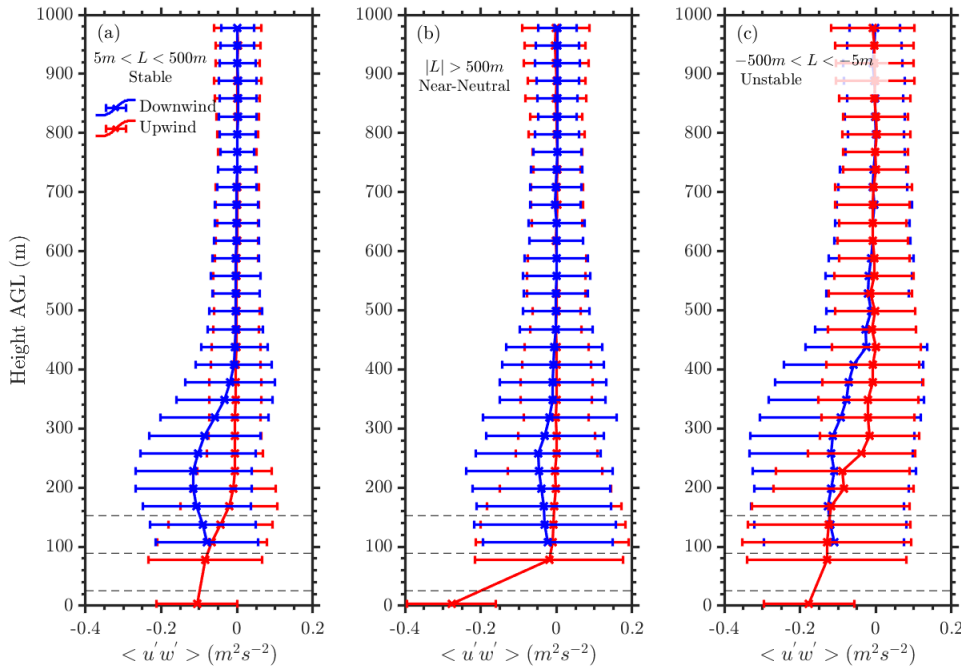


Figure 35. Median Momentum-momentum flux profiles at ~40 RD upwind (site A2) and 22 RD downwind (site H) of the King Plains wind farm during a) stable, b) near-neutral and c) unstable atmospheric conditions. The vertical extent of the wind turbine rotor layer is also shown with horizontal grey-dotted black lines. Near surface Obukhov length (L) is used to differentiate between different stability conditions. Error bars represent the sample standard deviation at respective heights. Measurements only from southerly wind directions, specifically from 166 deg-degrees to 190 deg-degrees, and from 17 March 2023 to 10 September 2023 are considered in this analysis.

5.3.2 Impact of low-level jets on wake recovery

Stable conditions produce low-level jets (LLJ)LLJs in the U.S. Great Plains (Berg et al., 2015, Krishnamurthy et al., 2021a) whose characteristics can modulate wind farm performance/power output (Gadde and Stevens, 2020). There are several definitions of low-level jet height (Z_{LLJ}) in the literature (Blackadar, 1959, Bonner 1968, Whiteman et al., 1997, Song et al., 2005, Kalverla et al., 2019, Debnath et al., 2020) but in this article is defined as per Song et al., 2005. The definition is based off two criteria, 1) wind speed maximum (i.e., low-level jet nose) is observed within the lowest 2-km and is greater than at least $>10 \text{ ms}^{-1}$, and 2) wind speed drop-off above the jet-nose is observed and above a set threshold. Three categories of the LLJs were identified based on varying thresholds of drop-off speeds and maximum nose wind speed (Song et al.,

2005), although in this analysis all LLJ categories were combined. [Figure 4](#)[Figure 6a](#) shows the distribution of various near-surface atmospheric stability classes during southerly wind directions (from 166 [degrees](#) to 190 [degrees](#)) [during LLJ events](#) and associated median Z_{LLJ} for each atmospheric stability class. It can be observed that lower Z_{LLJ} are typically associated with very stable or stable near-surface atmospheric conditions, while higher Z_{LLJ} are observed when the surface atmospheric stability is not stable, indicating a decoupled boundary layer (Vanderwende et al., 2015). Therefore, there could be confounding influences of the near surface stability and low-level jet influence on the wind farm wakes during such instances. [Figure 4](#)[Figure 6b](#) shows [low-level jet](#)[LLJ](#) nose wind speed as a function of median Z_{LLJ} per wind speed bin and hub-height wind speed [and Figure 4c shows \$Z_{LLJ}\$ as a function of hub-height wind speed](#). It is evident that higher the Z_{LLJ} , higher the jet nose wind speed and higher the hub-height wind speed. Overall, it is challenging to decipher various processes influencing wind farm wake recovery using observations but would be possible to isolate certain common features known to influence wind farm recovery (such as low-level jet height, or atmospheric stability or atmospheric boundary layer or hub-height wind speed) and study the variability observed during such select features.

Formatted: Font: 10 pt, Not Bold

As previously observed using historical measurements from the ARM SGP site, Z_{LLJ} generally falls within 500 m above ground level (Debnath et al, 2023). Since the scanning lidar measurements start from ~100 m above ground level, in this analysis we only evaluate [low-level jets](#)[LLJs](#) observed above the [rotor layer](#)[turbine hub-height](#) (> [127-110](#) m). Therefore, the observations are partitioned into two halves, a) $250 \text{ m} < Z_{LLJ} < 500 \text{ m}$ and b) [127-110](#) m < $Z_{LLJ} < 250 \text{ m}$. [The partitioning was driven by selecting a height near the wind turbine rotor layer \(25.5 m to 152.5 m\) that could be impacted by the wind turbine, considering the frequency of LLJ events from southerly wind directions \(which peaked around 250 m above ground level\), and the observed peak in momentum flux during stable conditions, which occurred approximately 250 m above ground level as shown in Figure 3.](#) [Figure 5](#)[Figure 7](#) shows vertical profiles of momentum flux and wind speed both upwind and downwind of a wind farm for different low-level jet heights (Z_{LLJ}) as mentioned above and further conditioned to only southerly wind directions (166 [degrees](#) to 190 [degrees](#)). During southerly LLJ events at King Plains wind farm, it is being observed that the transfer of momentum into the wake of the wind farm is a function of the LLJ height. Higher Z_{LLJ} is associated with larger momentum transfer within the wake and lower velocity deficit at 22 RD downwind. In short, the wake recovery is faster when the LLJ height is higher. This is mainly due to the shear generated turbulence below Z_{LLJ} and the enhanced momentum deficit developed due to the wind farm. The peak entrainment height is observed to marginally increase with higher Z_{LLJ} . These results support some of the hypotheses from previous LES model results on this topic (Gadde and Stevens, 2020). One unique feature that is observed when $127 \text{ m} < Z_{LLJ} < 250 \text{ m}$, is that the low-level jet height is modulated due to the presence of a wind farm downwind of the wind farm, wherein the Z_{LLJ} is consistently observed above the wind farm at 22 RD downwind. The downwind Z_{LLJ} is approximately equal to the height of the internal boundary layer (δ_{IBL}) generated due to the presence of the wind farm. In addition, during low-level jet conditions, Z_{LLJ} is typically assumed to be the top of the atmospheric boundary layer (δ , Liu and Liang 2010), as the turbulence above the Z_{LLJ} is negligible. [Figure 6](#)[Figure 8](#) shows a schematic of the interaction between the wind farm,

Formatted: Font: 10 pt, Not Bold

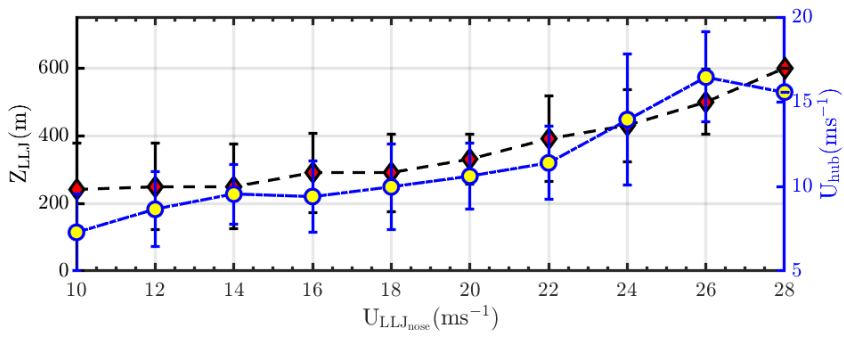
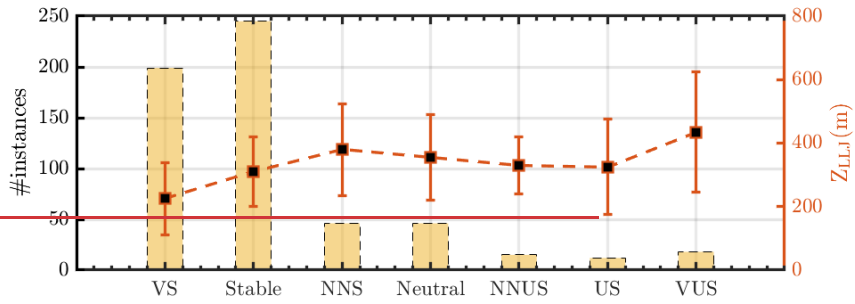
Formatted: Font: 10 pt, Not Bold

Formatted: Font: 10 pt, Not Bold

varying low-level jet heights and growth of the internal boundary layer due to the presence of the wind farm. Figure 7 illustrates the probability distribution of LLJ events at the upwind site (A2) and downwind site (H) of King Plains wind farm. The data reveal that the difference in LLJ height between the upwind and downwind sites is greater below approximately 250 to 300 m but diminishes at higher LLJ heights. Notably, there is a reduced frequency of LLJs observed downwind of the wind farm when LLJs occur below the rotor layer. Future research will focus on further analyzing the effects of LLJs that occur beneath the turbine rotor layer.

485

490



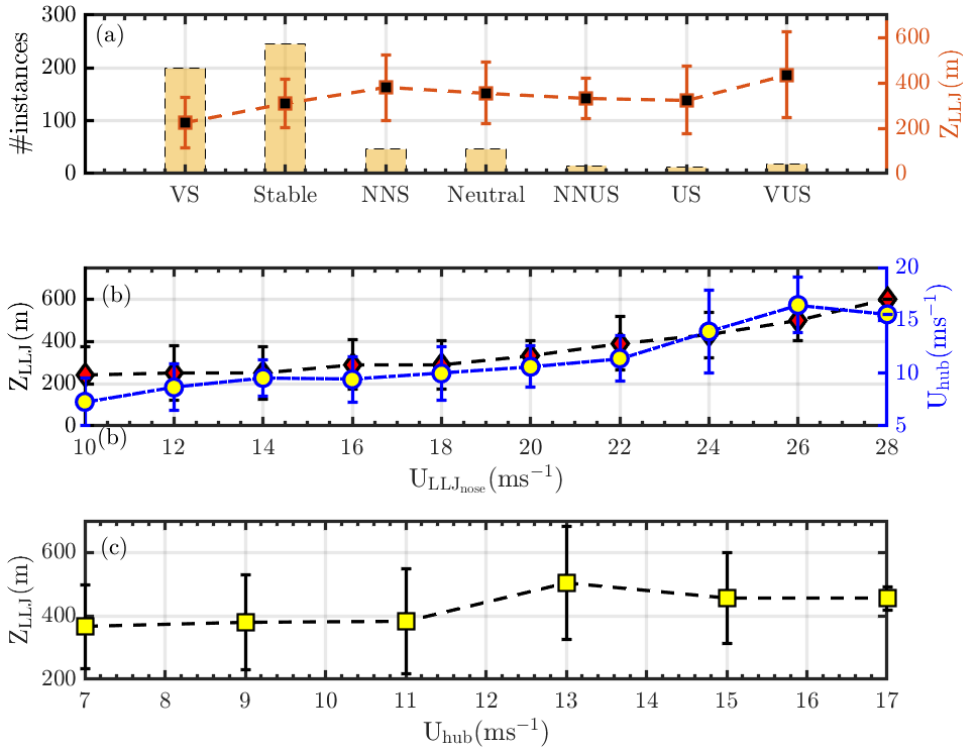
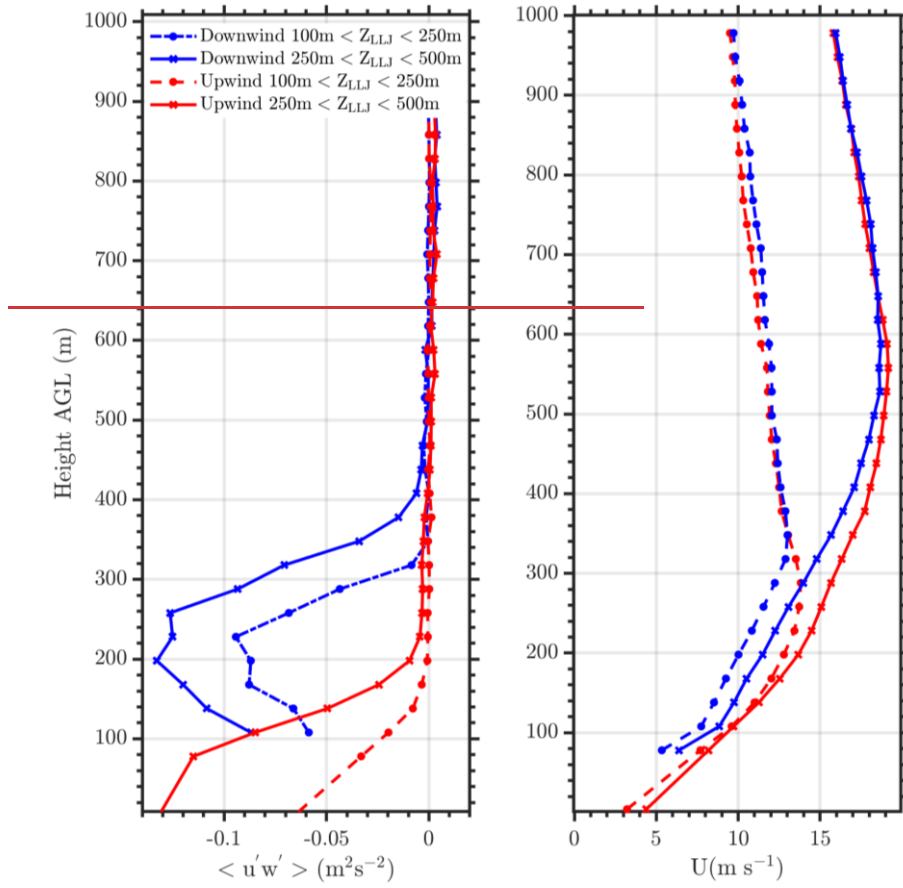


Figure 46. (top) Distribution of various atmospheric stability classes (VS – Very Stable, Stable, NNS – Near-Neutral Stable, Neutral, NNUS – Near-Neutral Unstable, US – Unstable, VUS – Very Unstable, as per Sathe et al., 2015) during LLJ events from southerly wind directions and associated Z_{LLJ} per stability class, and (bottom) median LLJ nose wind speed ($U_{LLJ,nose}$) as a function of Z_{LLJ} and Hubhub-height wind speed (U_{hub}) at the upwind site (site A2), and (c) Z_{LLJ} as a function of U_{hub} . The error bars indicate one standard deviation. Minimum Z_{LLJ} is 120-110 m and maximum Z_{LLJ} is 690 m AGL. Measurements only from southerly wind directions, especially from 166 deg-degrees to 190 degrees, and from 17 March 2023 to 10 September 2023 are considered in this analysis.

500



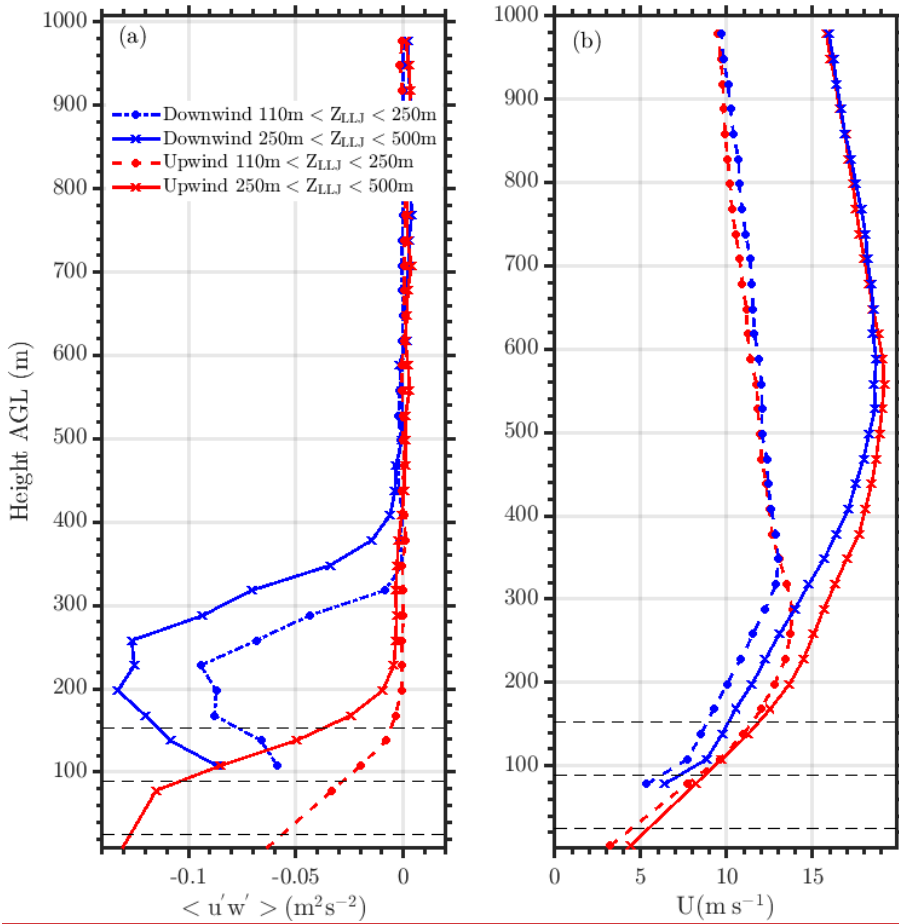
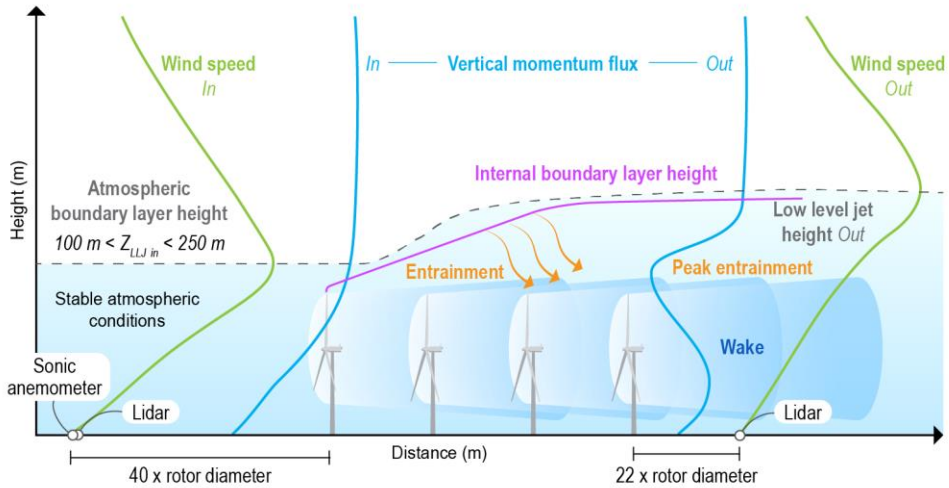


Figure 57. (left) Median streamwise momentum flux and (right) median horizontal wind speed profiles upwind (red, site A2) and downwind (blue, site H) of the King Plains wind farm during conditions when the Z_{LLJ} is less than 250 m AGL at the upwind location (dash-dotted) and Z_{LLJ} is between 250 m and 500 m AGL (star dotted). The vertical extent of the wind turbine rotor layer is also shown with horizontal dotted black lines. Measurements only from southerly wind directions, especially from 166 degrees to 190 degrees, and from 17 March 2023 to 10 September 2023 are considered in this analysis.

505



510

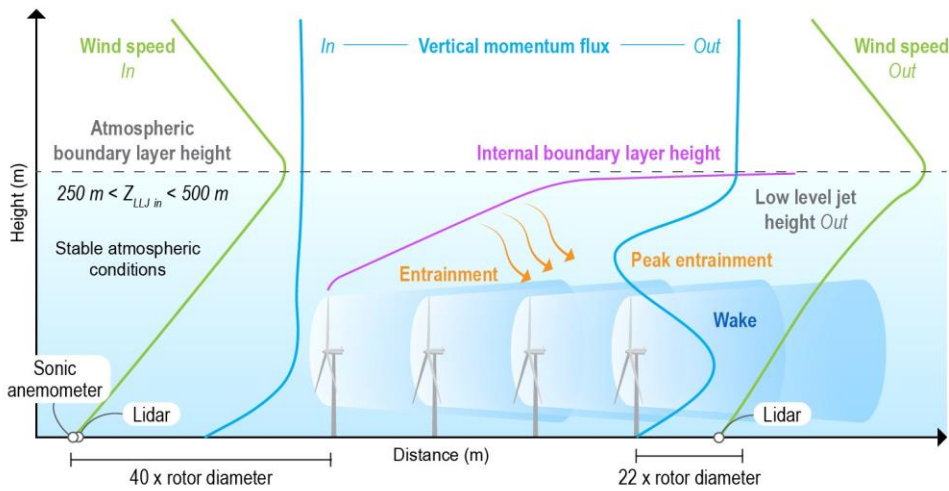
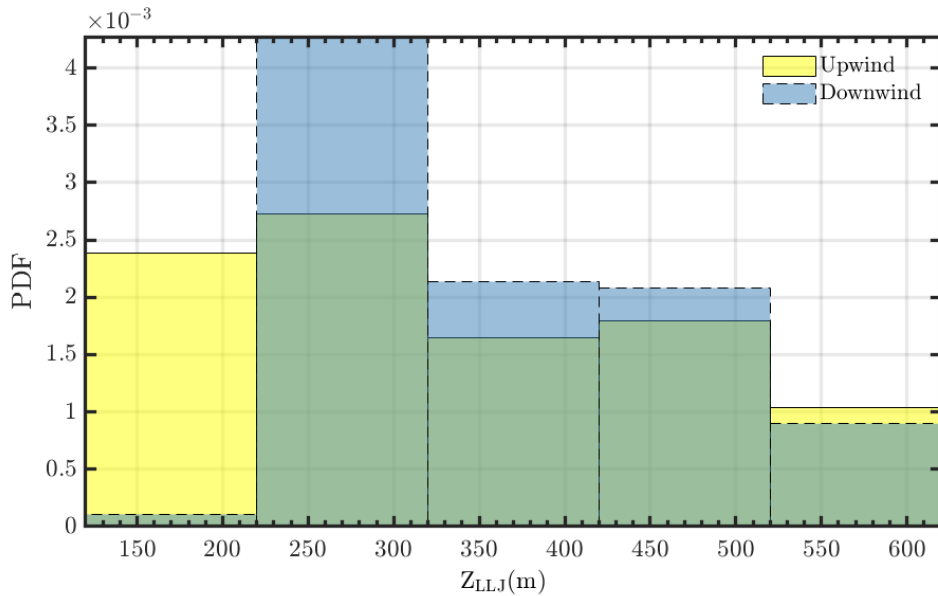


Figure 68. Schematic of impact of low-level jets on wind farm boundary layer when (top) $100\text{ m} < Z_{LLJ} < 250\text{ m}$ and (bottom) $250\text{ m} < Z_{LLJ} < 500\text{ m}$.



515 **Figure 7. Probability distribution of LLJ heights (Z_{LLJ}) upwind (site A2, yellow bar graph) and downwind (site H, blue bar graph) of the King Plains wind farm during southerly wind directions.**

53.3 Impact during varying shear and veer (non-LLJ) conditions on wake recovery

520 High wind shear and veer conditions are generally observed within a wind farm, but it is difficult to decouple the effects of shear or veer conditions compared to atmospheric stability conditions. Nonetheless, it would be helpful to observe any consistent trends during such conditions as they are known to impact power production of a wind farm (Murphy et al., 2020). In addition, such findings may be informative for wind farm control concepts that yaw wind turbines away from the predominant wind direction at hub-height but do not currently consider the wind veer within the rotor layer (Fleming et al., 2019). Figure 8Figure 9 and Figure 9Figure 10 show median profiles of momentum flux and horizontal wind speed both upwind and downwind of the King Plains wind farm during non-LLJ events for various shear and veer conditions, respectively. Estimates associated with positive and negative wind shear or veer conditions during southerly wind directions are provided.

Formatted: Font: 10 pt, Not Bold

Formatted: Font: 10 pt, Not Bold

Hub-height wind speed ($U(H)$) and shear exponent (α) are estimated by fitting a power-law vertical wind profile to the wind speed data available within the rotor layer (here from 90 m to 153 m, due to lack of observations below 90 m). The power-law fit is conveniently recast into a linear fit through a log transformation as shown in Eq. 74 below:

$$\log \log U(z) = \log \log U(H) + \alpha \log \log \left(\frac{z}{H} \right) \quad (74)$$

Where $\log \log \left(\frac{z}{H} \right)$ and $\log \log U(z)$ are the independent and dependent variables of the linear fit, respectively. Hub-height wind direction ($\phi(H)$) and veer ($\beta \equiv \frac{\partial \phi}{\partial z}$) are estimated in a similar fashion but using a linear wind veer model, as follows:

$$\phi(z) = \phi(H) + \beta(z - H) \quad (85)$$

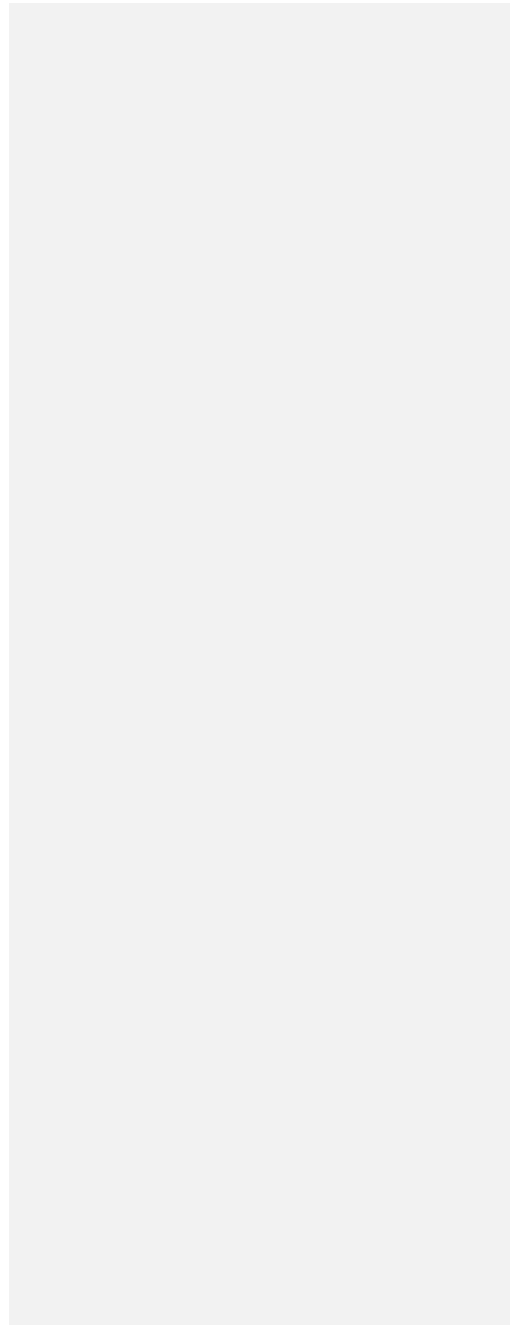
This approach for estimating hub height quantities has the advantage of leveraging all the available measurements while mitigating possible biases due to the lack of data in the lowest half of the rotor layer.

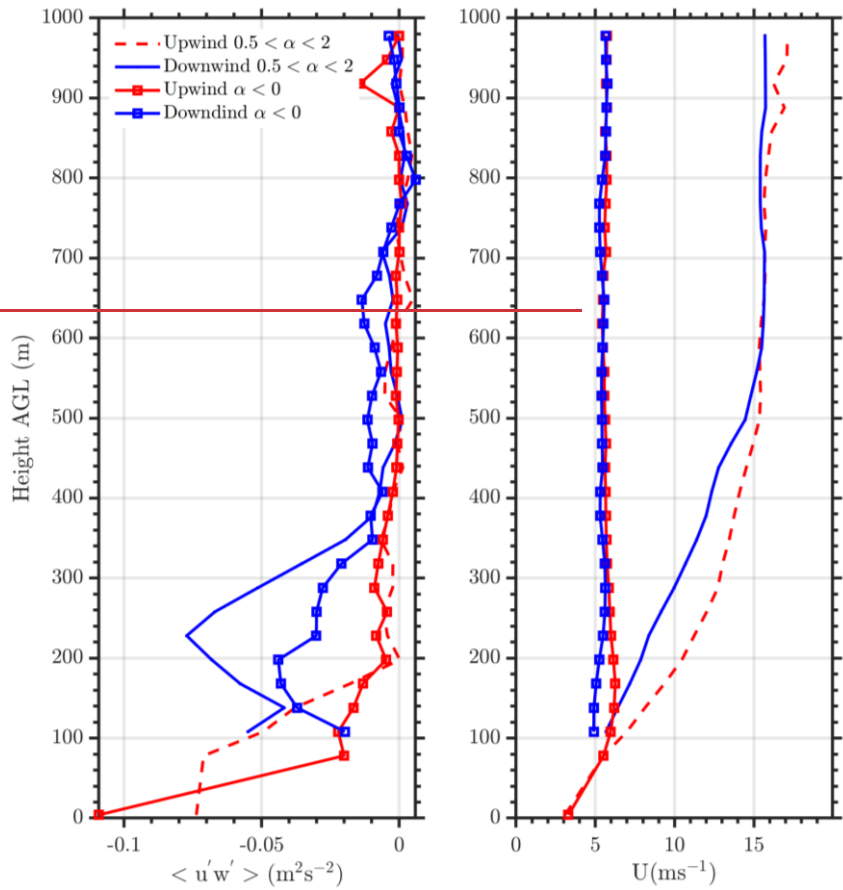
Certain trends are immediately observed for cases with positive or negative shear conditions (Figure 8Figure 9), where regardless of the wind shear profile, momentum deficits generated due to the wind farm are observed 22 RDs downwind of the wind farm. But both wind and momentum deficits are higher during conditions with high wind shear ($0.5 < \alpha < 2$) compared to low or negative wind shear ($\alpha \leq 0$) cases. Although a lower number of cases were recorded when the wind shear was low or negative at the King Plains wind farm compared to high wind shear cases. Median wind speeds at hub-height during both conditions are $\sim 5 \text{ ms}^{-1}$. For cases with negative wind shear, the median wind speed differences between upwind and downwind are negligible but a clear trend in median momentum flux profiles are observed. This raises an interesting question, according to the authors, what is a good metric to assess the extent of a wind farm wake? Traditionally it is expected for the wind speed to reach approximately 99% of the free stream wind speed, but in cases such as this where the wind speeds do reach near free stream, it could be erroneously assumed that the wind farm wake has completely been dissipated (Diath and Schulz-Stellenfleth, 2019). In reality, added turbulence due to the presence of a wind farm is not completely removed downwind of a wind farm under such circumstances. Additional research is needed to evaluate wind farm wake models or parameterization schemes during such canonical atmospheric conditions.

Although during cases with positive ($\beta > 0.1^\circ \text{ m}^{-1}$) and negative ($\beta < -0.1^\circ \text{ m}^{-1}$) wind veer conditions, median wind speeds are closer to the cut-in wind speeds of the GE 2.8 MW wind turbines and therefore no momentum flux deficits are observed (Figure 9Figure 10). Both high and low wind veer cases show that the median wind speeds are relatively low at King Plains wind farm. It is noted that the wind farm has also been observed to modify the wind direction downwind of a wind farm (not shown).

Formatted: Font: 10 pt, Not Bold

Formatted: Font: 10 pt, Not Bold





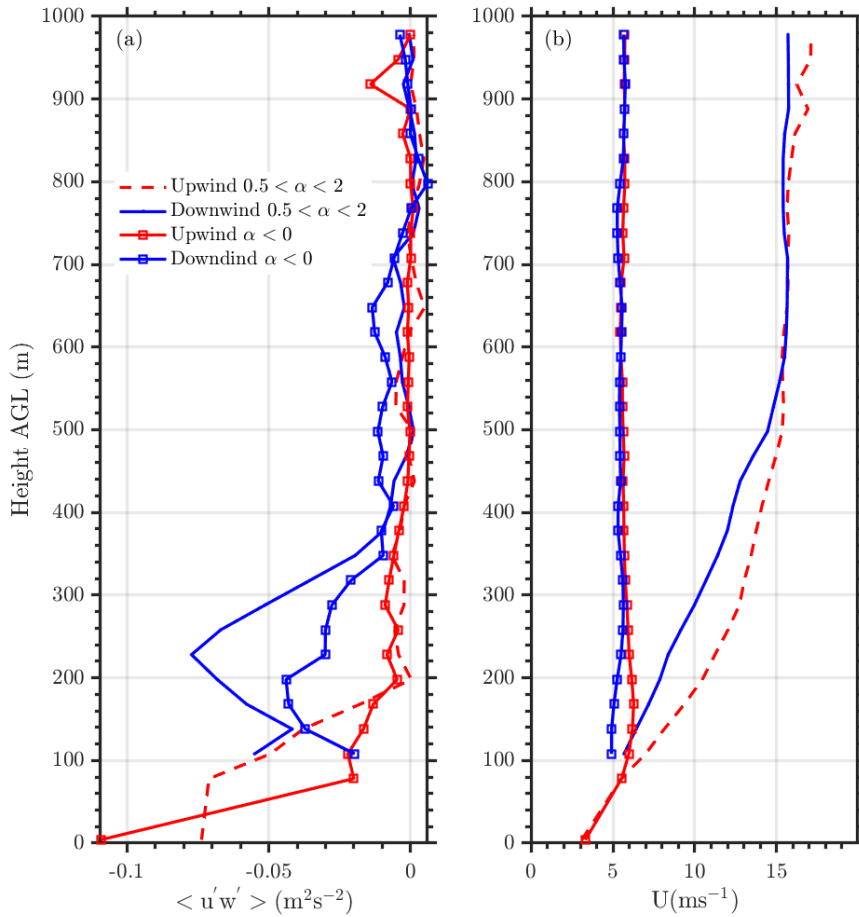
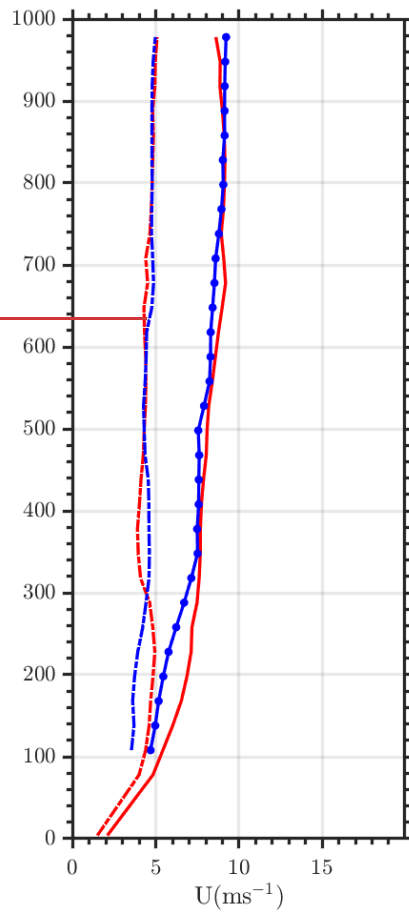
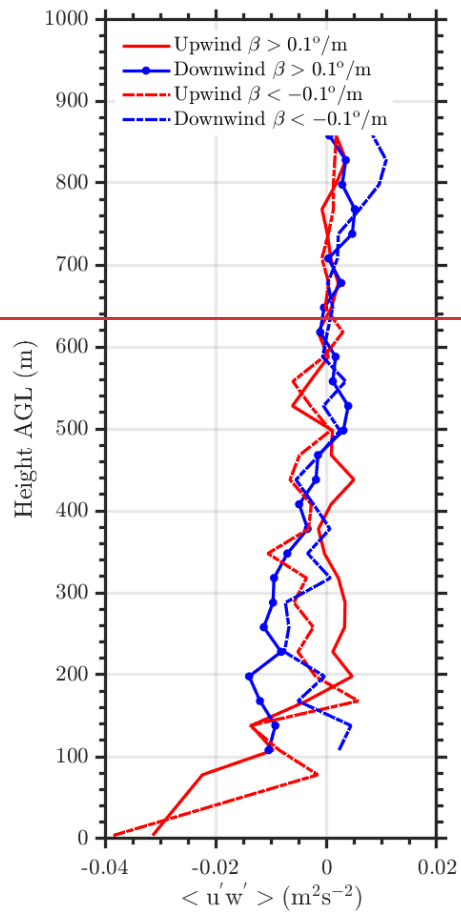
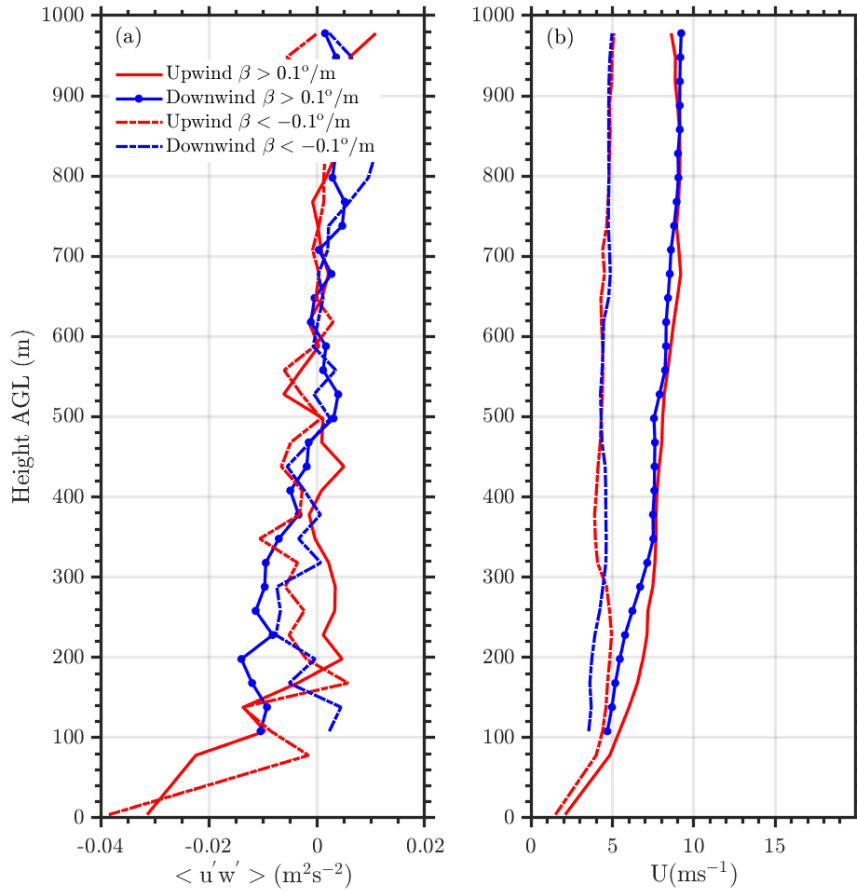


Figure 89. (a) Median (left) momentum flux and (right) horizontal wind speed profiles upwind (red) and downwind (blue) of the King Plains wind farm during high ($0.5 < \alpha < 2$, observed 53% of time) and negative ($\alpha \leq 0$, observed 2% of the time) wind shear conditions. Measurements only from southerly wind directions, especially from 166 degrees to 190 degrees, and from 17 March 2023 to 10 September 2023 are considered in this analysis.

565



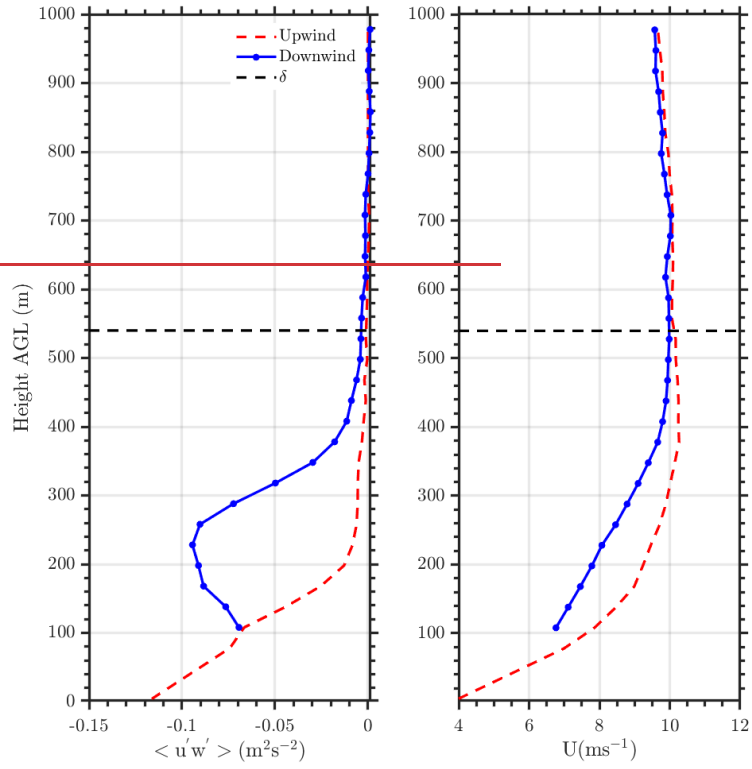


570 **Figure 210.** (left) Momentum flux and (right) horizontal wind speed profiles upwind (red) and downwind (blue) of the King Plains wind farm during high ($\beta > 0.1^\circ\text{m}^{-1}$, observed 28.5% of the time) and negative ($\beta < -0.1^\circ\text{m}^{-1}$, observed 1% of the time) wind veer conditions. Measurements only from southerly wind directions, especially from 166 degdegrees to 190 degdegrees, and from 17 March 2023 to 10 September 2023 are considered in this analysis.

575 5.3.4 Impact of ABL depth on wake recovery-Extent of wake within ABL

The atmospheric boundary-layer height (δ) is an important parameter for understanding the exchange of momentum, heat, and moisture between the free troposphere and the surface. Unfortunately, estimating δ can be challenging and there is limited consensus on the best approach to estimate δ from remote sensing instruments (Kottahaus et al., 2023). Typically, instruments such as scanning Doppler lidars or ceilometers are used to estimate δ (Tucker et al., 2009, Krishnamurthy et al., 2021b, Zhang et al., 2022). A ceilometer was deployed at the inflow site A1 and is used to estimate δ during southerly wind directions for this evaluation. The boundary layer (or mixing) height, provided by the Vaisala CL-31 BL-View software, is based on three different algorithms a) gradient method (where the algorithm detects the gradient in backscatter profile), b) profile method (where the algorithm determines the mixing height by fitting an idealized backscatter profile to the observed range-corrected ceilometer backscatter profiles) and c) merged gradient and profile fit method (Zhang et al., 2022). There are several filters applied to the data, such as cloud and precipitation filters, and additional outlier removal techniques (due to instrument noise). ~~Figure 10~~Figure 11 shows the median momentum flux and horizontal wind speed profiles during southerly wind directions and measurement co-located when concurrent ceilometer measurements were also available. The median δ (~540 m) at A1 from the ceilometer is below the height where both the median momentum flux estimates at sites A2 and H are near equal (~760 m). Therefore, it is observed that the median ceilometer δ does not accurately predict the height of the atmospheric boundary layer. There are several possible reasons for this, for example a) Ceilometer uses the gradient in backscatter aerosol concentrations to estimate δ , which might not always be the top of the boundary layer (Zhang et al., 2022), and b) upwind and downwind δ might be different due to the presence of the wind farm, therefore the δ estimated by the ceilometer well represents the δ at the inflow site (upwind momentum flux is observed to be close to zero). Above δ , the momentum flux deficits due to the presence of the wind farm are negligible. But overall, it is evident that the impact of the wind farms almost always reaches to the top of the atmospheric boundary layer. Therefore, it is important to model not only the wind turbine rotor layer with high vertical resolution but up to δ to accurately assess the impacts of wind farms and wake recovery. ~~We further recommend a long-term (1 year +) evaluation of wind farm wake models or parameterizations using long-term atmospheric flux observations through the boundary layer to assess the true performance of such models.~~

Formatted: Font: 10 pt, Not Bold



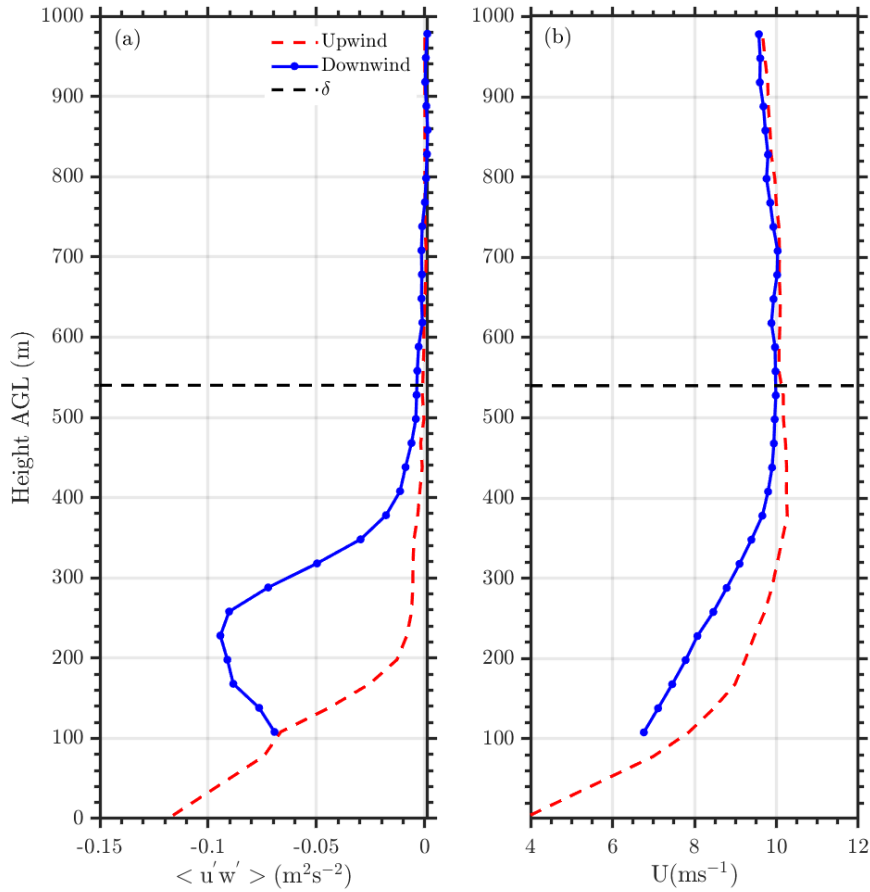


Figure 1014. (left) Momentum flux and (right) horizontal wind speed profiles upwind (red) and downwind (blue) of the King Plains wind farm for all atmospheric conditions. The median height of the ABL (δ) from ceilometer measurements is also shown. Measurements only from southerly wind directions, especially from 166 degrees to 190 degrees are considered in this analysis.

605

5.3.5 Impact of a gravity waves on wake recovery

Gravity waves and atmospheric bores are ubiquitous in the SGP region (Carbone et al., 1990; Davis et al., 2003; Ceeris et al., 2017). Although most frequently observed during nocturnal and stable atmospheric conditions, they vary significantly in their period and amplitude. These nocturnal convective systems typically accompany high winds, intense rain and/or hail and sometimes tornadoes (Maddox, 1980). The forecast skill of such atmospheric events is relatively low in both numerical weather prediction models and coarse grid climate models (Davis et al., 2003; Pritchard et al., 2011). They also typically include a low level jet within the atmospheric boundary layer, which supports the moisture transport above the stable boundary layer over SGP (Berg et al., 2015; Krishnamurthy et al., 2022). Primarily gravity waves create wave like oscillations in the atmosphere due to the presence of a density gradient and bore disturbances are shown to have a significant upward displacement of wind within the troposphere (Rottman and Simpson, 1989; Parson et al., 2019). Such wave like disturbances when reaching the surface, can create undulations in the mean winds depending on the period and wavelength of the wave. Mountain waves have previously been known to impact the power production of a wind farm (Draad et al., 2021) but the impact of propagating gravity waves on wake recovery is not very well understood.

Figure 11Figure 12 shows a time-height cross-section of vertical velocity as observed near ARM SGP central facility Doppler lidar (Newsom and Krishnamurthy, 2020, Krishnamurthy et al., 2021 a) on 24th July 2023 from 0300 to 0400 hours UTC (1900 to 2000 hours local time). The vertical velocity clearly shows wave-like features at approximately 800 m AGL, where we observe a positive and negative shift in vertical velocity. Figure 12Figure 13 shows median momentum flux and wind speed both upwind and downwind of the King Plains wind farm on 24th July 2023 from 0330 to 0400 UTC. The winds were predominantly southerly during this event with a veer of 0.0375 °/m from surface up to the top of the boundary layer. A nocturnal low-level jet was also observed at approximately 220 m AGL at the inflow site and the gravity wave is propagating above the nocturnal stable atmospheric boundary layer ($\sim Z_{LLJ}$). The peak-to-peak amplitude of the gravity wave is observed to be ~ 600 m, which spans from 400 m above ~ 1000 m.

As observed in Figure 12Figure 13, the momentum flux deficit is significantly enhanced above and within the wake of the King Plains wind farm. Estimates of vertical momentum flux deficits are more than three times compared to median estimates of momentum flux deficits observed during low-level jet conditions (see Figure 5Figure 7). Downwind, as previously noted, the peak of a low-level jet is observed to be displaced significantly above the wind farm which is a function of the enhanced mixing within the wind farm rotor layer. The higher the mixing, larger the entrainment, and higher the displacement of the low-level jet. Above the low-level jet, the gravity wave is observed to have an inverse effect, where the momentum flux is positive, entailing momentum is transferred upwards to the gravity wave. The positive or negative transfer of momentum near the gravity wave probably depends on the updrafts or downdrafts of the wave, but over the 30-min average observations the overall transfer of momentum is upwards. Therefore, further research is needed to understand if gravity waves are being dissipated faster due to the presence of a wind farm. The negative wind shear above the low-level jet could also add to the extraction of momentum from the wind farm. This reduces the intensity of the low-level jet and the

Formatted: Font: 10 pt, Not Bold

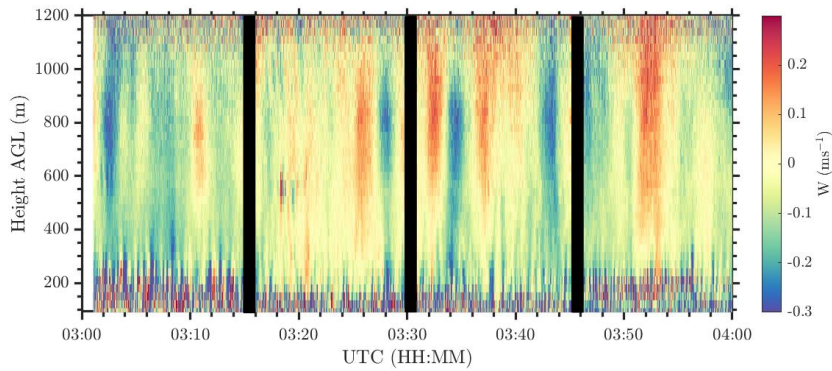
Formatted: Font: 10 pt, Not Bold

Formatted: Font: 10 pt, Not Bold

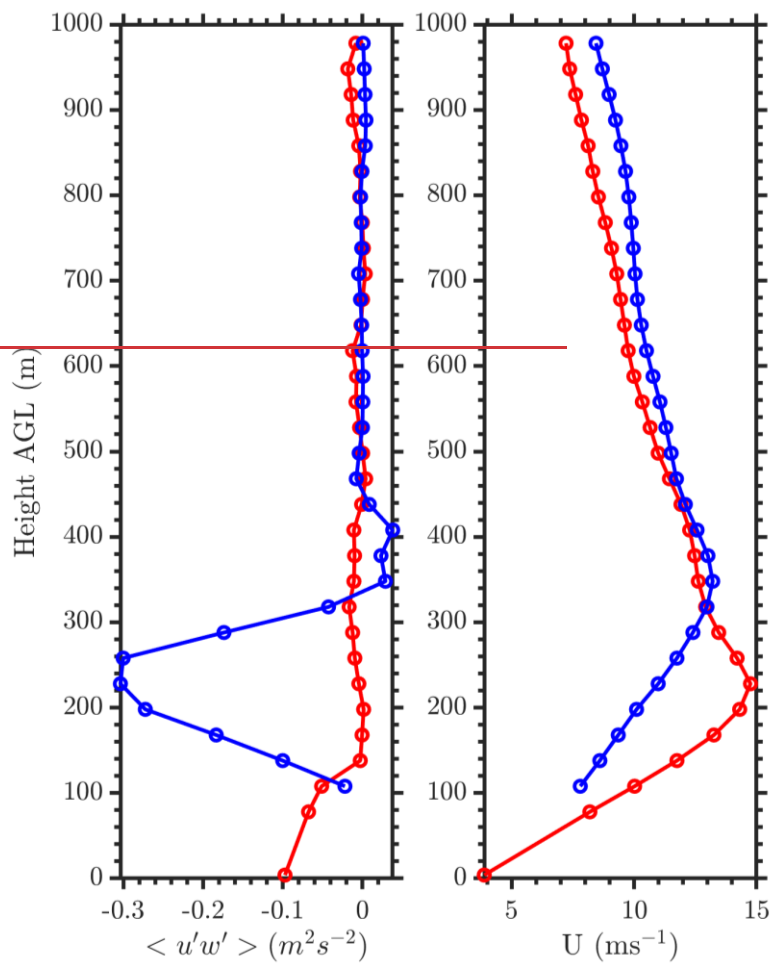
Formatted: Font: 10 pt, Not Bold

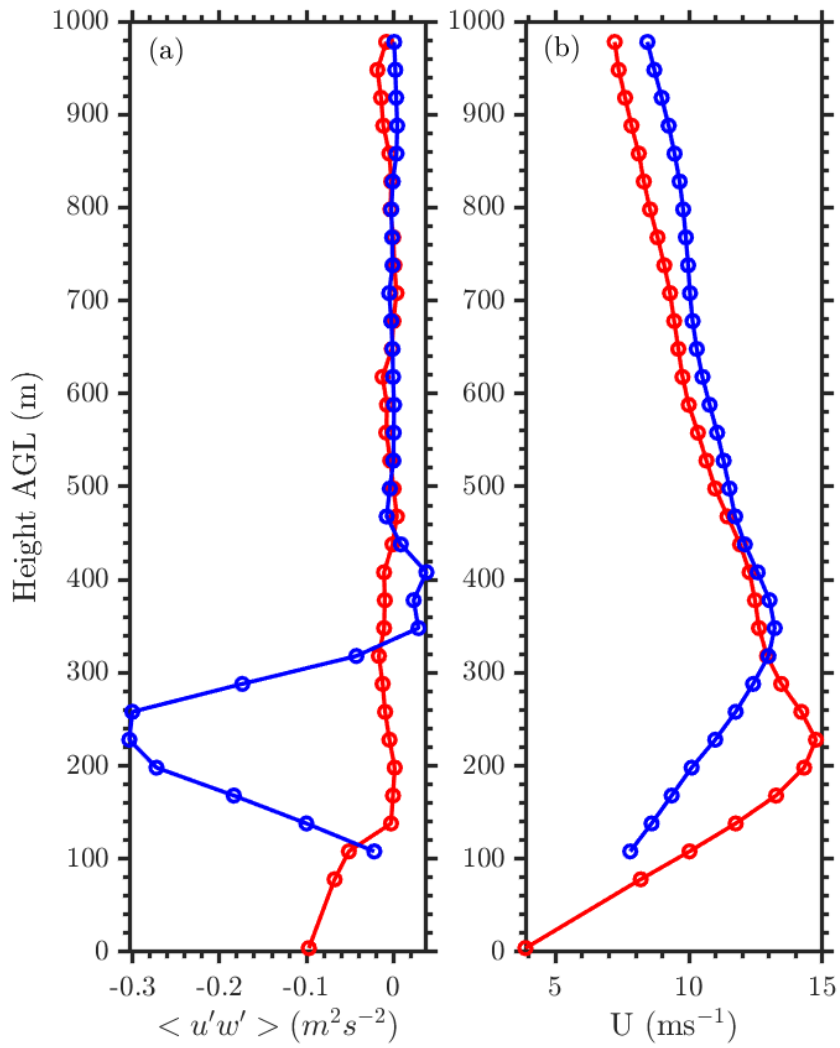
extracted momentum results in higher wind speeds above the low-level jet downwind of the wind farm. It is observed that in this case, the wind farm has significantly altered the winds not only within the δ , but also above and modulated the shape and intensity of the low-level jet. Additional analysis would be needed to see the spatial impact of wind farms during gravity wave propagation and power production. Next steps would be working towards a climatology of gravity waves in the region and its impact on wind farm performance.

645



650 **Figure 1142.** Time-height cross-section of vertical velocity (W) at ARM SGP central facility on 24-Jul-2023 from 03:00 to 04:00 UTC. The gaps in data every 15-minutes are when the lidar performs wind profiles (Newsom and Krishnamurthy, 2020).





655 **Figure 1243.** (a) Momentum flux and (b) horizontal wind speed profiles upwind (red) and downwind (blue) of the King Plains wind farm during a gravity wave event on 24 July 2023 at 3:30 UTC.

4 Comparisons of observed δ_{IBL} with theoretical estimates ~~Internal Boundary Layer Height~~

660 As discussed earlier, an internal boundary layer (δ_{IBL}) is developed due to a step change in surface roughness. Turbulence is expected to be higher within the internal boundary layer (downwind of the surface roughness) compared to inflow (upwind of the surface roughness). Wind farms create a step change in surface roughness and are known to develop internal boundary layers downwind of a wind farm (Calaf et al., 2013, Stevens and Meneveau, 2017). In addition to the roughness impacts of the wind turbines, the wind farm developed internal boundary layer is convolved with the wake of the wind turbines, which create additional momentum deficits downwind of the wind farm. Internal boundary layers can be estimated from a velocity profile, by identifying a kink in the velocity profile (Garratt et al., 1990). Although this method
665 provides a general trend, it is known to be not very accurate. An alternative technique, proposed in Stevens 2016, is being implemented here, where the difference in streamwise momentum flux profiles upwind and downwind of a surface roughness change are used to estimate the growth of the internal boundary layer. ~~Internal boundary layer height (δ_{IBL}) can be estimated using the difference between inflow and outflow momentum flux profiles.~~ Vertical momentum flux is responsible for the influx of momentum into the wake of a wind farm. Larger streamwise momentum flux deficits above the wind farm
670 are mainly observed due to turbulence and shear generated by the wind turbines. Wind turbine wakes enhance vertical mixing above a wind farm, which results in a downward flow of momentum. The internal boundary layer height (δ_{IBL}) is the height when the upwind and downwind momentum flux estimates are approximately within 1 – 5% of each other above the wind farm.

675 Wind farm δ_{IBL} is typically capped by δ but ~~previously LES modelling results has been previously have shown in large-eddy simulations~~ to penetrate the upwind δ during ~~low-level jets~~ LLJs (Gadde and Stevens, 2020). As shown earlier, model formulations exist to estimate δ_{IBL} downwind of a wind farm (Eq. 2). But the growth constant and wind farm surface roughness formulations have been fine-tuned based on large-eddy simulations, and as per the author's knowledge, no significant analysis on the validation of such formulations have been conducted so far using real-world observations. This article does not attempt to do that comparison in detail but is the start of such comparisons. The model formulations (Eq. 2)
680 are sensitive to ~~upwind~~ surface roughness in the presence of a wind farm (z_0, h_i) estimates and the growth constant (C), which can significantly vary δ_{IBL} estimates within the model (sensitivity analysis not shown for brevity). The model formulations also do not explicitly restrict the growth of δ_{IBL} but are implicitly treated in models where the sub-grid scale mixing does not exceed δ , especially during stable atmospheric conditions.

685 Figure 13~~Figure 14~~ shows the difference in estimates of δ_{IBL} from observations and model formulations (Eq. 2) only during stable atmospheric conditions and in the presence of a low-level jet. Since we have higher confidence in δ_{IBL} during

Formatted: Font: 10 pt, Not Bold

these cases and δ already represents the top of the LLJ height, this also avoids introducing additional uncertainty from Ceilometer δ observations. Some of the inputs to model formulations are provided by real-world observations, such as the lidar 10-minute average wind speed at hub-height, inflow surface friction velocity and roughness from sonic anemometers, thrust curve of the GE 2.8 MW wind turbine, and average wind turbine spacing in southerly wind directions. Given real-world inputs, the median δ_{IBL} difference between the model and observations is approximately 50 m, i.e., the model underestimates the δ_{IBL} . ~~Although there are~~ During some extreme cases ($\Delta\delta_{IBL} > 200$ m), ~~where~~ the model does not behave due to ~~nonin-~~consistent wind directions for a sustained period (several hours), ~~the overall performance of the model can be considered satisfactory.~~ Additional research is needed with large-eddy simulations or numerical weather prediction models with real-world forcing to assess the recovery and growth of δ_{IBL} at an operational wind farm.

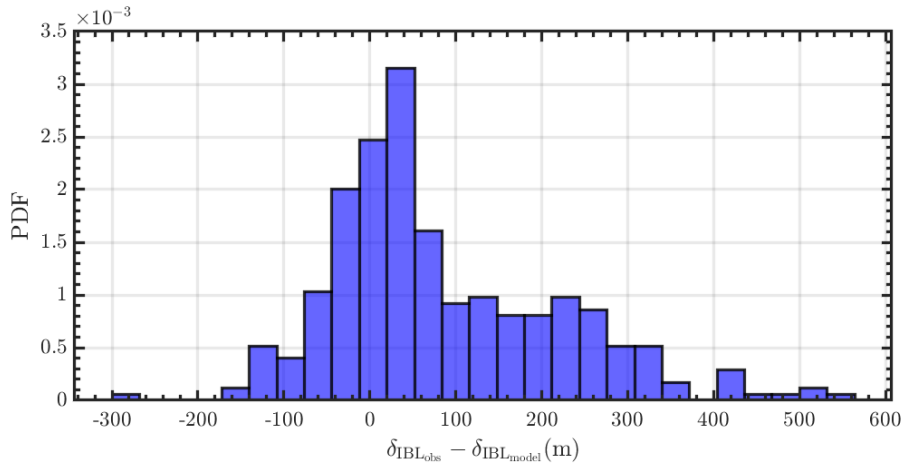


Figure 1314. Probability distribution of δ_{IBL} difference between observations and a semi-empirical model (Eq. 2) during stable atmospheric conditions and in presence of a low-level jet.

5 Conclusions

These novel observations reveal the temporal and spatial variability of momentum balance within and above the wind farm wakes during regional specific atmospheric conditions. Profiles also show the growth of the internal boundary layer and allow quantification of the accuracy of current large-eddy simulation-based approximations in estimating the growth of the internal boundary layer (IBL).

The momentum balance surrounding a wind farm ~~can may~~ impact wake recovery. The greater the momentum flux the faster the wake velocity recovers to a freestream value. Wind farm wakes are known to propagate long distances during stable atmospheric conditions, and thereby the vertical momentum flux added due to the presence of the wind farm is more persistent at downwind locations and varies with the diurnal cycle. Stable conditions also produce ~~low-level jets~~ LLJs in the US Great Plains, which are known to impact the performance and power output of commercial wind farms. ~~Figure 6~~ Figure 14 shows a schematic of the impact of varying low-level jet height on wind farm wake recovery and modulation of the flow downwind of the wind farm. ~~In addition, presence, and size of an internal boundary layer above the wind farm will impact the momentum exchange between the ABL and the wind farm boundary layer.~~ Therefore, long-term measurements of vertical momentum flux upwind and downwind of a wind farm can provide a holistic view of the physical mechanisms behind wake recovery during various atmospheric conditions. In this study, we have evaluated the impact of wake recovery using long-term observations of vertical momentum flux through the boundary layer during a variety of atmospheric conditions. Overall, some highlights of the observations are mentioned below:

Formatted: Font: 10 pt, Not Bold

~~1. Wakes propagate longest during stable atmospheric conditions (see Figure 5),~~

~~2.1. Wind farms alter low-level jet characteristics downwind of the wind farm, by elevating the height of the jet above the wind farm (see Figure 5~~ Figure 7 and ~~Figure 6~~ Figure 8),

Formatted: Font: 10 pt, Not Bold

~~3.2. The height of the low-level jet significantly impacts wind farm wake recovery downwind, with higher low-level jet heights resulting in faster wake recovery (see Figure 5~~ Figure 7 and ~~Figure 6~~ Figure 8),

Formatted: Font: 10 pt, Not Bold

~~4.3. Negative wind shear during non-LLJ cases show short wake propagation at 22 RD downwind of a wind farm,~~

Formatted: Font: 10 pt, Not Bold

~~5.4. Wind farm wake impacts are observed through the δ (see Figure 10~~ Figure 11),

Formatted: Font: 10 pt, Not Bold

~~6.5. Gravity waves enhances wake recovery and accelerates winds above the low-level jet downwind of a wind farm (see Figure 12~~ Figure 13), and lastly,

Formatted: Font: 10 pt, Not Bold

~~7.6. Large-eddy simulation-based theoretical δ_{IBL} models perform well show a large spread given real-world inputs of the atmosphere and turbine.~~

Finally, we have highlighted several areas of research in this article that still need to be conducted to understand the dynamics of the wind farm influenced atmospheric boundary layer, mentioned below:

1. Additional comparisons between LES models and observations are required to further evaluate the wake recovery processes within a wind farm wake. Since most mesoscale wake model parameterizations are assessed using outputs from LES models.
2. It is important to model not only the wind turbine rotor layer with high vertical resolution but up to the top of the δ to accurately assess the impacts of wind farms and wake recovery (as shown in Figure 10). As it is important to understand the entrainment of winds from the ABL to the wind farm wake boundary layer.
3. Recommend long term (1-year +) evaluation of wind farm wake models or parameterizations using long-term atmospheric flux observations through the boundary layer to assess the true performance of such models.

4. Analysis would be needed to see the spatial impact of wind farms during gravity wave propagation and power production.
5. Research is needed with large-eddy simulations or numerical weather prediction models with real-world forcing to assess the recovery and growth of δ_{IBL} at an operational wind farm.

Future work will focus on developing a methodology to classify gravity waves in the region and assess the power production impacts in the presence of gravity waves at the King Plains wind farm site. In addition, comparison of observations and models will be conducted to refine wind farm parameterization schemes within numerical weather models.

Appendix A: Flux estimation algorithms and approach

Herein we provide details of the algorithms used to estimate momentum fluxes from surface-based anemometers and scanning Doppler lidars; and a methodology to estimate the height of the internal boundary layer from upwind and downwind momentum flux profiles.

A.1 Momentum flux estimates from sonic anemometers

Sonic anemometers are considered a standard for estimating atmospheric turbulence parameters (Wilczak et al., 2001, Wilczak et al., 2019, Fernando et al., 2019). Three-dimensional (3-D) acoustic anemometers provide measurements of winds and temperature at high temporal frequency (≥ 20 Hz), which supports calculation of higher order statistics with good accuracy (Cook and Sullivan, 2020). The sign conventions of the 3-D winds vary for different manufacturers and for Gill Sonic anemometers, which were deployed for this project, the sign conventions are defined as positive for upward vertical wind component (w) and upward atmospheric fluxes, u wind component (North-South) is positive towards North and v wind component (East-West) is positive towards the West. The raw and flux data files are generated as per Cook and Sullivan, (2020), and contain 30-minutes of post-processed data and estimates of turbulent fluxes. The sonic data is post-processed by first applying a de-spiking procedure (Goring and Nikora, 2002) to remove any data anomalies and a 2-axis coordinate rotation is performed (Wilczak et al., 2001), which ensures $\langle w \rangle = \langle v \rangle = 0$ and $\langle u_s \rangle = U$, where U is the mean wind speed, u_s is the streamwise component and $\langle \cdot \rangle$ is a 30-minute temporal average. To estimate the fluxes, the average of each variable is estimated over a 30-minute (non-overlapping) window and no detrending of the data is performed to estimate the velocity fluctuations. The stress tensor is then computed using 30-minute measurements of velocity fluctuations and assumed to be statistically stationary over the averaging window. Momentum flux estimates from sonic anemometer data were calculated using the eddy-covariance method (Stull, 1988).

A.2 Momentum flux profiles from Doppler lidars

A brief description of the method to estimate momentum flux profiles from lidars is given below (Eberhard et al., 1989; Mann et al., 2010). The radial velocity (v_r) equation of a Doppler lidar is given by:

$$v_r(R, \theta) = u(R) \sin \varphi \cos \theta + v(R) \sin \varphi \sin \theta + w(R) \cos \varphi \quad (A.1)$$

where, R is the range, φ is the half-opening angle of the conical scan (30°), θ is the azimuthal direction of the lidar beam (0 degrees is North), and $\{u, v, w\}$ are the wind components at each range-gate center. The variance of v_r is given by

$$\sigma^2[v_r(R, \theta)] = \sigma_u^2 \sin^2 \varphi \cos^2 \theta + \sigma_v^2 \sin^2 \varphi \sin^2 \theta + \sigma_w^2 \cos^2 \varphi + 2\langle u'v' \rangle \sin^2 \varphi \cos \theta \sin \theta + 2\langle u'w' \rangle \cos \varphi \sin \varphi \cos \theta + 2\langle v'w' \rangle \cos \varphi \sin \varphi \sin \theta \quad (A.2)$$

where $\langle \rangle$ represents 30-minute averaging and $\{u', v', w'\}$ are the velocity fluctuations. One can estimate the streamwise momentum flux components ($\langle u'w' \rangle$) by calculating the radial velocity variance in the upwind and downwind directions over 30-minutes (Eberhard et al., 1989; Mann et al., 2010), which is then given by

$$\langle u'w' \rangle = \frac{\sigma^2[v_{r \text{ down}}] - \sigma^2[v_{r \text{ up}}]}{2 \sin 2\varphi} \quad (A.3)$$

where, $\sigma^2[v_{r \text{ down}}]$ and $\sigma^2[v_{r \text{ up}}]$ are the radial velocity variances from the nearest downwind and upwind azimuth angles relative to the mean wind direction, respectively and ϕ is the mean wind direction. The nearest up and down radial velocities from the azimuth angles are picked for each 30-minute sample and given range-gate wind direction estimate. It can be noted from Eq. 5A.3 that in a positively sheared turbulent flow, $\sigma^2(v_{r \text{ up}}[v_{r \text{ up}}]) > \sigma^2(v_{r \text{ down}}[v_{r \text{ down}}])$, i.e., the upwind variances, are typically larger than downwind variances. The effect of measurement volume is not considered in this analysis and has been shown to have a minimal impact on the streamwise momentum flux measurements for Doppler lidars (Mann et al., 2010).

For evaluating the accuracy of the algorithm, continuous Velocity Azimuth Display (VAD) scans at the same elevation and azimuth angles are required to calculate the variance of the radial velocity along each beam. From October 8, 2020, to January 14, 2021, continuous eight-point Planned Position Indicator (PPI) scans ($\Delta \text{az} = 45^\circ$ and $\text{el} = 60^\circ$) were conducted at the Atmospheric Radiation Measurement (ARM) Southern Great Plains (SGP) Central Facility to support an ongoing field campaign. The mean wind direction (ϕ) at each height is calculated using the approach of Newsom et al. (2017), wherein a chi-square distribution is fit to estimate the horizontal wind vector. Each beam was averaged for 6 seconds to provide a robust estimate of radial velocity and study the effect of noise from individual radial velocity measurements (Frehlich et al., 2001). This averaging could underestimate the variance observed by the lidar. During this study, each 360-degree wind profile was completed in ~ 1 minute. This provided the ability to calculate variance of radial velocity along each beam and the momentum flux profile using Eq. 5A.3. Momentum flux estimates from sonic anemometer data on a 60 m

lower were calculated using the eddy correlation method (Stull, 1988). Along-wind momentum flux ($\langle u'w' \rangle$) estimates from the sonic anemometer at 60 m and lidar at 75 m from southerly wind directions are shown in the Figure A1a.

805

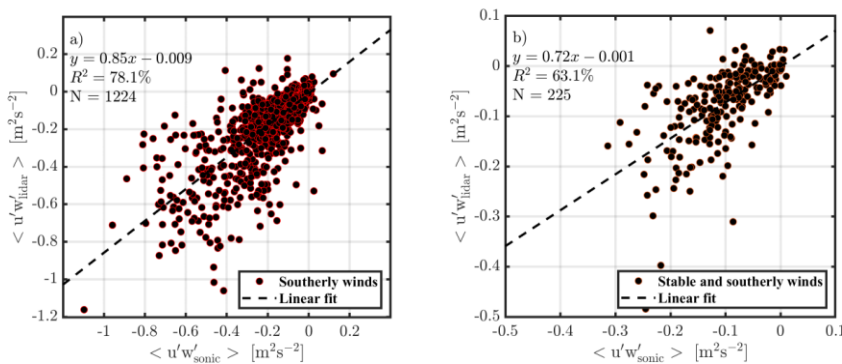
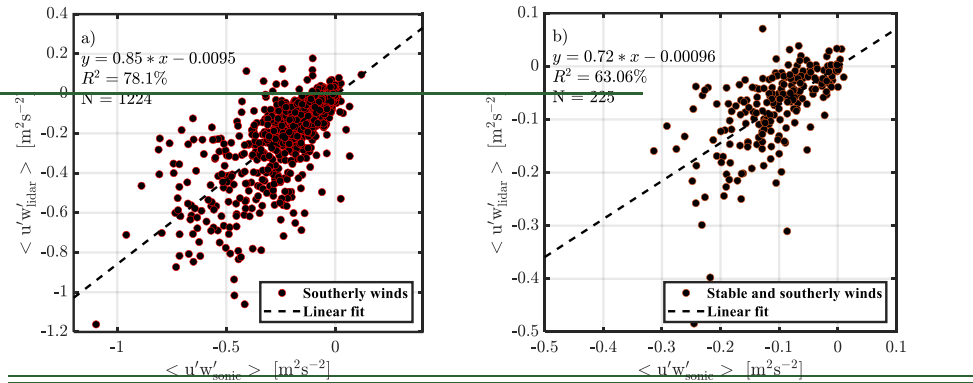


Figure A1: 30-minute averaged along-wind momentum flux ($\langle u'w' \rangle$) measurements from lidar at 75 m and sonic at 60 m AGL from October 8, 2020, to January 14, 2021 at ARM SGP central facility, for a) southerly wind directions under all atmospheric conditions and b) southerly wind directions under very stable atmospheric conditions ($10 m < L < 150 m$). A linear fit between the measurements ($y = m^*x + c$), coefficient of determination (R^2), and number of samples (N) are also shown. The X-axis scaling for (a) and (v) are different.

810

Doppler lidar $\langle u'w' \rangle$ measurements are observed to correlate reasonably well to sonic anemometer $\langle u'w' \rangle$ measurements, with slope of 0.85 and a coefficient of determination of ~78%. To quantify the effect of stable atmospheric

815

conditions on the accuracy of lidar derived momentum flux estimates, the stability of the atmosphere was determined using the Obukhov length, L , given by

$$L = \frac{u_*^3 T}{kg(w'^2 \theta'_v)}$$

where T is the air temperature, g is the acceleration due to gravity, and $(w'\theta'_v)$ is the kinematic heat flux. During stable atmospheric conditions, given the amount degree of stratification within the lidar probe volume, the lidar could be measuring very different atmospheric conditions compared to a sonic anemometer. Figure A1b shows measurements from southerly wind directions and very stable atmospheric conditions ($10 \text{ m} < L < 150 \text{ m}$). The coefficient of determination is observed to reduce during stable conditions to ~63%, although the wind speeds are observed to correlate well under all conditions. The transfer of momentum is lowest in stable atmospheric conditions and therefore smaller momentum flux estimates are observed. From a purely statistical standpoint, the smaller magnitude of the fluxes also contributes to reducing the coefficient of determination, since under these conditions the contribution of instrumental and statistical noise to the physical variability of relatively larger. The scatter between lidar and sonic measurements are primarily due to (a) 15 m vertical and ~250 m horizontal separations between sonic anemometer and lidar measurements, (b) low temporal sampling of the lidar measurements, and (c) spatial averaging of the lidar pulse (range-gate = 30 m). These effects amplify during stable atmospheric conditions and result in larger scatter between measurements. Previous observations of momentum flux from profiling Doppler lidars have shown a similar accuracy when compared to sonic anemometers at various heights above ground level (Mann et al., 2010). Overall, the performance of the algorithm is expected to be adequate for the analysis being conducted in this article.

835 Codes and data statement

All the data is publicly available on the ARM Discovery webpage (<https://adc.arm.gov/discovery/#/>) or on the Wind Data Hub (<https://www.a2e.energy.gov>). The lidar data DOI at site H is 10.21947/2283040 and site A2 is 10.5439/1890922, sonic anemometer data DOI is 10.21947/1899850, finally, ceilometer data at site A1 DOI is 10.21947/2221789.

840 Author contribution

RK and RN designed the experiments. RK developed the code and performed the analysis. RK prepared the manuscript with contributions from all co-authors. CK and PM acquired funding for the analysis. SL, MP, NH, DC, DF, NB assisted in collecting data from various sensors and supported with data analysis.

Competing interests

845 The authors declare that they have no conflict of interest.

Acknowledgements

The authors would like to thank the ARM infrastructure for making the data publicly available and to all the mentors for maintaining and processing the instrument data. The authors would also like to thank the Wind Data Hub team for making the AWAKEN field campaign data publicly available. PNNL is operated for DOE by the Battelle Memorial Institute under
850 Contract DE-AC05-76RLO1830. This work was authored in part by the National Renewable Energy Laboratory, operated by Alliance for Sustainable Energy, LLC, for the U.S. Department of Energy (DOE) under Contract No. DE-AC36-08GO28308. Funding provided by the U.S. Department of Energy Office of Energy Efficiency and Renewable Energy Wind Energy Technologies Office. The views expressed in the article do not necessarily represent the views of the DOE or the U.S. Government. The U.S. Government retains and the publisher, by accepting the article for publication, acknowledges
855 that the U.S. Government retains a nonexclusive, paid-up, irrevocable, worldwide license to publish or reproduce the published form of this work, or allow others to do so, for U.S. Government purposes. [We also thank the two reviewers for their detailed comments to the manuscript.](#)

References

- 860 Abkar, M., and Porté-Agel, F.: The effect of free-atmosphere stratification on boundary-layer flow and power output from very large wind farms, *Energies*, 6(5), 2338-2361, doi:10.3390/en6052338, 2013.
- Abkar, M., and Porté-Agel, F.: Mean and turbulent kinetic energy budgets inside and above very large wind farms under conventionally-neutral condition, *Renewable Energy*, 70, 142-152, doi:10.1016/j.renene.2014.03.050, 2014.
- Abkar, M., and Porté-Agel, F.: Influence of atmospheric stability on wind-turbine wakes: A large-eddy simulation study, *Physics of fluids*, 27(3), 035104, doi:10.1063/1.4913695, 2015.
- 865 Allaerts, D., and Meyers, J.: Boundary-layer development and gravity waves in conventionally neutral wind farms, *Journal of Fluid Mechanics*, 814, 95-130, doi: 10.1017/jfm.2017.11, 2017.
- Baidya Roy, S., Pacala, S. W., and Walko, R. L.: Can large wind farms affect local meteorology?, *Journal of Geophysical Research: Atmospheres*, 109(D19), doi: 10.1029/2004JD004763, 2004.
- Barthelmie, R. J., Hansen, K. S., and Pryor, S. C.: Meteorological controls on wind turbine wakes, *Proceedings of the IEEE*, 101(4), 1010-1019, doi: 10.1109/JPROC.2012.2204029, 2012.
- 870 Berg, L. K., Riihimäki, L. D., Qian, Y., Yan, H., and Huang, M.: The low-level jet over the southern Great Plains determined from observations and reanalyses and its impact on moisture transport, *Journal of Climate*, 28(17), 6682-6706, doi: 10.1175/JCLI-D-14-00719.1, 2015.
- Berg, L. K., Newsom, R. K., and Turner, D. D.: Year-long vertical velocity statistics derived from Doppler lidar data for the continental convective boundary layer. *Journal of Applied Meteorology and Climatology*, 56(9), 2441-2454, doi: 10.1175/JAMC-D-16-0359.1, 2017.
- Bodini, N., Lundquist, J. K., & Moriarty, P.: Wind plants can impact long-term local atmospheric conditions. *Scientific reports*, 11(1), 22939, doi:10.1038/s41598-021-02089-2, 2021.
- 880 Bonin, T. A., Choukulkar, A., Brewer, W. A., Sandberg, S. P., Weickmann, A. M., Pichugina, Y. L., Banta, R. M., Oncley, S. P., and Wolfe, D. E.: Evaluation of turbulence measurement techniques from a single Doppler lidar, *Atmos. Meas. Tech.*, 10, 3021–3039, <https://doi.org/10.5194/amt-10-3021-2017>, 2017.
- Brower, M.: *Wind resource assessment: a practical guide to developing a wind project*. John Wiley and Sons, 2012.

Calaf, M., Parlange, M. B., and Meneveau, C.: Large eddy simulation study of scalar transport in fully developed wind-turbine array boundary layers, *Physics of Fluids*, 23(12), 126603, doi: 10.1063/1.3663376, 2011.

885 [Carbone, R.E., Conway, J.W., Crook, N.A. and Moncrieff, M.W.: The generation and propagation of a nocturnal squall line. Part I: Observations and implications for mesoscale predictability. Monthly Weather Review, 118\(1\), pp.26-49, doi: 10.1175/1520-0493\(1990\)118<0026:TGAPOA>2.0.CO;2, 1990.](#)

Cook DR and RC Sullivan.: Eddy Correlation Flux Measurement System (ECOR) Instrument Handbook. Ed. by Robert Stafford, ARM user facility. DOE/SC-ARM/TR-052. 10.2172/1467448, 2020.

890 [Davis, C. A., Manning, K. W., Carbone, R. E., Trier, S. B., & Tuttle, J. D.: Coherence of warm-season continental rainfall in numerical weather prediction models. Monthly Weather Review, 131\(11\), 2667-2679, doi: 10.1175/1520-0493\(2003\)131<2667:COWCRI>2.0.CO;2, 2003.](#)

895 Debnath, M., Moriarty, P., Krishnamurthy, R., Bodini, N., Newsom, R., Quon, E., Lundquist, JK, Letizia, S, Jungo, V, and Klein, P: Characterization of wind speed and directional shear at the AWAKEN field campaign site. *Journal of Renewable and Sustainable Energy*, 15(3), doi: 10.1063/5.0139737, 2023.

[Djath, B., Schulz-Stellenfleth, J., and Cañadillas, B.: Impact of atmospheric stability on X-band and C-band Synthetic Aperture Radar imagery of offshore windpark wakes. Journal of Sustainable and Renewable Energy, 10\(4\), 2018, doi: 10.1063/1.5020437.](#)

900 [Djath, B., and Schulz-Stellenfleth, J.: Wind speed deficits downstream offshore wind parks - A new automatised estimation technique based on satellite synthetic aperture radar data, Meteorologische Zeitschrift, 28\(6\), 499–515, doi: 10.1127/metz/2019/0992, 2019.](#)

[Draxl, C., Worsnop, R. P., Xia, G., Pichuegina, Y., Chand, D., Lundquist, J. K., Sharp, J., Wedam, G., Wilczak, J. M., and Berg, L. K.: Mountain waves can impact wind power generation. Wind Energy Science, 6\(1\), 45-60, doi: 10.5194/wes-6-45-2021, 2021.](#)

905 Eberhard, W. L., Cupp, R. E., and Healy, K. R.: Doppler lidar measurement of profiles of turbulence and momentum flux, *Journal of Atmospheric and Oceanic Technology*, 6(5), 809-819, doi:10.1175/1520-0426, 1989.

Fernando, H. J. S., Mann, J., Palma, J. M. L. M., Lundquist, J. K., Barthelmie, R. J., Belo-Pereira, M., ... and Wang, Y.: The Perdigo: Peering into microscale details of mountain winds, *Bulletin of the American Meteorological Society*, 100(5), 799-819, doi: 10.1175/BAMS-D-17-0227.1, 2019.

910 Frehlich, R.: Coherent Doppler lidar signal covariance including wind shear and wind turbulence, *Appl. Opt.*, 33, 6472–6481, doi:10.1364/AO.33.006472, 1994.

Frehlich, R.: Estimation of velocity error for Doppler lidar measurements, *J. Atmos. Ocean. Tech.*, 18, 1628–1639, doi:10.1175/1520-0426(2001)018<1628:EOVEFD>2.0.CO;2, 2001.

Frehlich, R. and Cornman, L.: Estimating spatial velocity statistics with coherent Doppler lidar, *J. Atmos. Ocean. Tech.*, 19, 355–366, doi:10.1175/1520-0426-19.3.355, 2002.

915 Frehlich, R., Meillier, Y., Jensen, M. L., Balsley, B., and Sharman, R.: Measurements of boundary layer profiles in an urban environment, *J. Appl. Meteorol. Clim.*, 45, 821–837, doi:10.1175/JAM2368.1, 2006

Fleming, P., King, J., Dykes, K., Simley, E., Roadman, J., Scholbrock, A., ... and Brake, D.: Initial results from a field campaign of wake steering applied at a commercial wind farm—Part 1. *Wind Energy Science*, 4(2), 273-285, doi: 10.5194/wes-4-273-2019, 2019.

920 Gadde, S. N., and Stevens, R. J.: Interaction between low-level jets and wind farms in a stable atmospheric boundary layer, *Physical Review Fluids*, 6(1), 014603, doi:10.1103/PhysRevFluids.6.014603, 2001.

Garratt, J. R.: The internal boundary layer—A review, *Boundary-layer meteorology*, 50, 171-203, doi:10.1007/BF00120524, 1990.

- 925 [Geerts, B., Parsons, D., Ziegler, C.L., Weckwerth, T.M., Biggerstaff, M.I., Clark, R.D., Coniglio, M.C., Demoz, B.B., Ferrare, R.A., Gallus Jr, W.A. and Haghi, K.: The 2015 plains elevated convection at night field project. Bulletin of the American Meteorological Society, 98\(4\), pp.767-786, doi: 10.1175/BAMS-D-15-00257.1, 2017.](#)
- Goring, D. G., and Nikora, V. I.: Despiking acoustic Doppler velocimeter data, Journal of hydraulic engineering, 128(1), 117-126, doi: 10.1061/(ASCE)0733-9429(2002)128:1(117), 2002.
- 930 Gustafson Jr, W. I., Vogelmann, A. M., Li, Z., Cheng, X., Dumas, K. K., Endo, S., ... and Xiao, H.: The large-eddy simulation (LES) Atmospheric Radiation Measurement (ARM) Symbiotic Simulation and Observation (LASSO) activity for continental shallow convection. Bulletin of the American Meteorological Society, 101(4), E462-E479, doi:10.1175/BAMS-D-19-0065.1, 2020.
- 935 Hansen, K. S., Barthelmie, R. J., Jensen, L. E., and Sommer, A.: The impact of turbulence intensity and atmospheric stability on power deficits due to wind turbine wakes at Horns Rev wind farm, Wind Energy, 15(1), 183-196, doi:10.1002/we.512, 2012.
- Hirth, B. D., Schroeder, J. L., Gunter, W. S., and Guynes, J. G.: Measuring a utility-scale turbine wake using the TTUKa mobile research radars, Journal of Atmospheric and Oceanic Technology, 29(6), 765-771, doi:10.1175/JTECH-D-12-00039.1, 2012.
- 940 Hoen, B.D., Diffendorfer, J.E., Rand, J.T., Kramer, L.A., Garrity, C.P., and Hunt, H.E.: United States Wind Turbine Database (ver. 3.3, January 14, 2021): U.S. Geological Survey, American Clean Power Association, and Lawrence Berkeley National Laboratory data release, <https://doi.org/10.5066/F7TX3DN0>, 2018.
- Kotthaus, S., Bravo-Aranda, J. A., Collaud Coen, M., Guerrero-Rascado, J. L., Costa, M. J., Cimini, D., ... and Haefelin, M.: Atmospheric boundary layer height from ground-based remote sensing: a review of capabilities and 945 limitations, Atmospheric Measurement Techniques, 16(2), 433-479, doi:10.5194/amt-16-433-2023, 2023.
- Krishnamurthy, R., Calhoun, R., Billings, B., and Doyle, J.: Wind turbulence estimates in a valley by coherent Doppler lidar, Meteorological Applications, 18(3), 361-371, doi:10.1002/met.263, 2011.
- Krishnamurthy, R., Reuder, J., Svardal, B., Fernando, H. J. S., and Jakobsen, J. B.: Offshore wind turbine wake characteristics using scanning Doppler lidar. Energy Procedia, 137, 428-442, doi:10.1016/j.egypro.2017.10.367, 2017.
- 950 [Krishnamurthy, R., Newsom, R.K., Chand, D., and Shaw, W.J.: Boundary layer climatology at arm southern great plains \(No. PNNL-30832\). Pacific Northwest National Lab. \(PNNL\), Richland, WA \(United States\). Doi: 10.2172/1778833.2021a.](#)
- Krishnamurthy, R., Newsom, R. K., Berg, L. K., Xiao, H., Ma, P. L., and Turner, D. D.: On the estimation of boundary layer heights: a machine learning approach. Atmospheric Measurement Techniques, 14(6), 4403-4424, 955 doi:10.5194/amt-14-4403-2021, 2021b.
- Krishnamurthy, R., Fernando, H. J. S., Alappattu, D., Creegan, E., and Wang, Q.: Observations of offshore internal boundary layers, Journal of Geophysical Research: Atmospheres, e2022JD037425, doi:10.1029/2022JD037425, 2023.
- [Lampert, A., et al.: In situ airborne measurements of atmospheric and sea surface parameters related to offshore wind parks in the German Bight. Earth System Science Data, 12\(2\), 935-946, 2020, doi: 10.5194/essd-12-935-2020.](#)
- 960 Liu, S. and Liang, X.Z.: Observed diurnal cycle climatology of planetary boundary layer height, Journal of Climate, 23(21), pp.5790-5809, doi:10.1175/2010JCLI3552.1, 2010.
- Lu, H., and Porté-Agel, F.: On the impact of wind farms on a convective atmospheric boundary layer, Boundary-Layer Meteorology, 157(1), 81-96, doi: 10.1007/s10546-015-0049-1, 2015.
- 965 Lundquist, J. K., DuVivier, K. K., Kaffine, D., and Tomaszewski, J. M.: Costs and consequences of wind turbine wake effects arising from uncoordinated wind energy development, Nature Energy, 4(1), 26-34, doi:10.1038/s41560-018-0281-2, 2019.
- Lothon, M., Lenschow, D. H., and Mayor, S. D.: Doppler lidar measurements of vertical velocity spectra in the convective planetary boundary layer, Boundary-layer meteorology, 132(2), 205-226, doi:10.1007/s10546-009-9398-y, 2009.

- 970 [Maddox, R.A., 1980. Mesoscale convective complexes. Bulletin of the American Meteorological Society, pp.1374-1387.](#)
- Mann, J., Peña, A., Bingöl, F., Wagner, R., and Courtney, M. S.: Lidar scanning of momentum flux in and above the atmospheric surface layer, *Journal of Atmospheric and Oceanic Technology*, 27(6), 959-976, doi:10.1175/2010JTECHA1389.1, 2010.
- 975 Mather, J. H., and Voyles, J. W.: The ARM Climate Research Facility: A review of structure and capabilities, *Bulletin of the American Meteorological Society*, 94(3), 377-392, doi:10.1175/BAMS-D-11-00218.1, 2013.
- Miller, L. M., and Keith, D. W.: Climatic impacts of wind power, *Joule*, 2(12), 2618-2632, doi:10.1016/j.joule.2018.09.009, 2018.
- Monin, A. S., and Obukhov, A. M.: Basic laws of turbulent mixing in the surface layer of the atmosphere, *Contrib. Geophys. Inst. Acad. Sci. USSR*, 151(163), e187, 1954.
- 980 [Moriarty P., N. Bodini, P. Brugger, L.A. Goldberger, N. Hamilton, T. Herges, B. Hirth, et al.: Overview of Preparation for the American Wake Experiment \(AWAKEN\), Journal of Renewable and Sustainable Energy, In Press, 2024.](#)
- Murphy, P., Lundquist, J. K., and Fleming, P.: How wind speed shear and directional veer affect the power production of a megawatt-scale operational wind turbine, *Wind Energy Science*, 5(3), 1169-1190, doi:10.5194/wes-5-1169-2020, 2020.
- 985 Newsom K., Brewer W. A., Wilczak J. M., Wolfe D., Oncley S. P., Lundquist J. K.: Validating Precision Estimates in Horizontal Wind Measurements from a Doppler Lidar, *Atmospheric Measurement Techniques* 10(3):1229-1240, doi:10.5194/amt-10-1229-2017, 2017.
- Newsom, R. K. and Krishnamurthy, R.: Doppler lidar (DL) handbook (No. DOE/SC-ARM/TR-101). DOE Office of Science Atmospheric Radiation Measurement (ARM) Program (United States). Available online: http://www.arm.gov/publications/tech_reports/handbooks/dl_handbook. Pdf, 2020.
- 990 Nygaard, N. G., and Newcombe, A. C.: Wake behind an offshore wind farm observed with dual-Doppler radars, In *Journal of Physics: Conference Series* (Vol. 1037, No. 7, p. 072008). IOP Publishing, doi:10.1088/1742-6596/1037/7/072008, 2018.
- 995 [Parsons, D. B., Lillo, S. P., Rattray, C. P., Bechtold, P., Rodwell, M. J., and Bruce, C. M.: The role of continental mesoscale convective systems in forecast busts within global weather prediction systems. Atmosphere, 10\(11\), 681, doi:10.3390/atmos10110681, 2019.](#)
- Pearson, G., Davies, F., and Collier, C.: Remote sensing of the tropical rain forest boundary layer using pulsed Doppler lidar, *Atmospheric Chemistry and Physics Discussions*, 10(2), doi:10.5194/acp-10-5891-2010, 2010.
- 1000 Peña, A., Hasager, C. B., Gryning, S.-E., Courtney, M., Antoniou, I., and Mikkelsen, T.: Offshore wind profiling using light detection and ranging measurements, *Wind Energy*, 12, 105–124, doi:10.1002/we.283, 2009.
- [Platis, A., Siedersleben, S. K., Bange, J., Lampert, A., Bärfuss, K., Hankers, R., Cañadillas, B., Foreman, R., Schulz-Stellenfleth, J., Djath, B., Neumann, T., and Emeis, S.: First in situ evidence of wakes in the far field behind offshore wind farms. Scientific Reports, 8, 2163, doi:10.1038/s41598-018-20389-v, 2018.](#)
- 1005 [Pritchard, M. S., Moncrieff, M. W., & Somerville, R. C.: Orographic propagating precipitation systems over the United States in a global climate model with embedded explicit convection. Journal of the Atmospheric Sciences, 68\(8\), 1821-1840, doi: 10.1175/2011JAS3699.1, 2011.](#)
- Rajewski, D. A., Takle, E. S., Lundquist, J. K., Oncley, S., Prueger, J. H., Horst, T. W., ... and Doorenbos, R. K.: Crop wind energy experiment (CWEX): observations of surface-layer, boundary layer, and mesoscale interactions with a wind farm, *Bulletin of the American Meteorological Society*, 94(5), 655-672, doi:10.1175/BAMS-D-11-00240.1, 2013
- 1010 [Rottman, J. W., and Simpson, J. E.: The formation of internal bores in the atmosphere: A laboratory model. Quarterly Journal of the Royal Meteorological Society, 115\(488\), 941-963, doi:10.1002/qj.49711548809, 1989.](#)
- Sathe, A., and Mann, J.: A review of turbulence measurements using ground-based wind lidars. *Atmospheric Measurement Techniques*, 6(11), 3147-3167, doi:10.5194/amt-6-3147-2013, 2013.

- 1015 Sathe, A., Mann, J., Vasiljevic, N., and Lea, G.: A six-beam method to measure turbulence statistics using ground-based wind lidars, *Atmos. Meas. Tech.*, 8, 729–740, <https://doi.org/10.5194/amt-8-729-2015>, 2015.
- [Schneemann, J., Rott, A., Dörenkämper, M., Steinfeld, G., and Kühn, M.: Cluster wakes impact on a far-distant offshore wind farm's power. *Wind Energy Science*, 5, 29–49, doi:10.5194/wes-5-29-2020, 2020.](#)
- 1020 [Shaw, W. J., Berg, L. K., Debnath, M., Deskos, G., Draxl, C., Ghate, V. P., Hasager, C. B., Kotamarthi, R., Mirocha, J. D., Muradyan, P., Pringle, W. J., Turner, D. D., and Wilczak, J. M.: Scientific challenges to characterizing the wind resource in the marine atmospheric boundary layer. *Wind Energy Science*, 7, 2307–2334, doi:10.5194/wes-7-2307-2022, 2022.](#)
- Siedersleben, S. K., Lundquist, J. K., Platis, A., Bange, J., Bärfuss, K., Lampert, A., and Emeis, S.: Micrometeorological impacts of offshore wind farms as seen in observations and simulations, *Environmental Research Letters*, 13(12), 124012, doi:10.1088/1748-9326/aaea0b, 2018.
- 1025 Smalikho, I., Köpp, F., and Rahm, S.: Measurement of atmospheric turbulence by 2- μ m Doppler lidar. *Journal of Atmospheric and Oceanic Technology*, 22 (11), 1733-1747, doi: 10.1175/JTECH1815.1, 2015.
- Smith, C. M., Barthelmie, R. J., and Pryor, S. C.: In situ observations of the influence of a large onshore wind farm on near-surface temperature, turbulence intensity and wind speed profiles, *Environmental Research Letters*, 8(3), 034006, doi: 10.1088/1748-9326/8/3/034006, 2013.
- 1030 [Stevens, R. J.: Dependence of optimal wind turbine spacing on wind farm length. *Wind energy*, 19\(4\), 651-663, doi:10.1002/we.1857, 2016.](#)
- [Stull, R.B., 1988. Boundary layer clouds. In *An Introduction to Boundary Layer Meteorology* \(pp. 545-585\). Dordrecht: Springer Netherlands.](#)
- 1035 Syed, A. H., Mann, J., Platis, A., and Bange, J.: Turbulence structures and entrainment length scales in large offshore wind farms, *Wind Eng. Sci.*, 8, 125–139, <https://doi.org/doi:10.5194/wes-8-125-2023>, 2023.
- [Taylor, P.: On wind and shear stress profiles above a change in surface roughness. *Quarterly Journal of the Royal Meteorological Society*, 95\(403\), 77–91, doi:10.1002/qj.49709540306, 1969.](#)
- 1040 Tucker, S. C., Senff, C. J., Weickmann, A. M., Brewer, W. A., Banta, R. M., Sandberg, S. P., ... and Hardesty, R. M.: Doppler lidar estimation of mixing height using turbulence, shear, and aerosol profiles, *Journal of atmospheric and oceanic technology*, 26(4), 673-688, doi:10.1175/2008JTECHA1157.1, 2009.
- VerHulst, C., and Meneveau, C.: Large eddy simulation study of the kinetic energy entrainment by energetic turbulent flow structures in large wind farms. *Physics of Fluids*, 26(2), 025113, doi:10.1063/1.4865755, 2014.
- Wang, D., Giangrande, S. E., Feng, Z., Hardin, J. C., and Prein, A. F.: Updraft and downdraft core size and intensity as revealed by radar wind profilers: MCS observations and idealized model comparisons, *Journal of Geophysical Research: Atmospheres*, 125(11), e2019JD031774, doi:10.1029/2019JD031774, 2020.
- 1045 Wilczak, J. M., Oncley, S. P., and Stage, S. A.: Sonic anemometer tilt correction algorithms, *Boundary-layer meteorology*, 99, 127-150, doi:10.1023/A:1018966204465, 2001.
- Wilczak, J. M., Stoelinga, M., Berg, L. K., Sharp, J., Draxl, C., McCaffrey, K., ... and White, A. B.: The second wind forecast improvement project (WFIP2): Observational field campaign, *Bulletin of the American Meteorological Society*, 100(9), 1701-1723, doi:10.1175/BAMS-D-18-0035.1, 2019.
- 1050 Wildmann, N., Bodini, N., Lundquist, J. K., Bariteau, L., and Wagner, J.: Estimation of turbulence dissipation rate from Doppler wind lidars and in situ instrumentation for the Perdígão 2017 campaign, *Atmos. Meas. Tech.*, 12, 6401–6423, <https://doi.org/10.5194/amt-12-6401-2019>, 2019.
- 1055 Yang, D., Meneveau, C., and Shen, L.: Large-eddy simulation of offshore wind farm. *Physics of Fluids*, 26(2), 025101, doi: 10.1063/1.4863096, 2014.
- Zhan, L., Letizia, S., and Valerio Iungo, G., LiDAR measurements for an onshore wind farm: Wake variability for different incoming wind speeds and atmospheric stability regimes, *Wind Energy*, 23(3), 501-527, doi:10.1002/we.2430, 2020.
- 1060 Zhang, D., Comstock, J., and Morris, V.: Comparison of planetary boundary layer height from ceilometer with ARM radiosonde data, *Atmos. Meas. Tech.*, 15, 4735–4749, <https://doi.org/10.5194/amt-15-4735-2022>, 2022.